Infrared Forcing by Greenhouse Gases

W. A. van Wijngaarden[1] and W. Happer [2]

[1]*Department of Physics and Astronomy, York University, Canada*
[2]*Department of Physics, Princeton University, USA*

June 18, 2019

Abstract

We review how the atmospheric temperatures and the concentrations of Earth's five most important, naturally-occurring greenhouse gases, H_2O, CO_2, O_3, N_2O and CH_4 control the cloud-free, thermal radiative fluxes from the Earth to outer space. Computations based on the line intensities HITRAN data base alone, with no absorption continuums, are used to evaluate fluxes and intensities for greenhouse-gas concentrations similar to those of the year 2019. Calculated top-of-the atmosphere spectral intensities are in excellent quantitative agreement with satellite measurements at various latitudes. Also calculated are per-molecule forcings in a hypothetical, optically thin atmosphere, where there is negligible saturation of the absorption bands, or interference of one type of greenhouse gas with others. Then the per-molecule forcings are of order 10^{-22} W for H_2O, CO_2, O_3, N_2O and CH_4. For current atmospheric concentrations, the per-molecule forcings of the abundant greenhouse gases H_2O and CO_2 are suppressed by four orders of magnitude from optically-thin values because of saturation of the strong absorption bands and interference from other greenhouse gases. The forcings of the less abundant greenhouse gases, O_3, N_2O and CH_4, are also suppressed, but much less so. For current concentrations, the per-molecule forcings are two to three orders of magnitude greater for O_3, N_2O and CH_4, than those of H_2O or CO_2. Doubling the current concentrations of CO_2, N_2O or CH_4 only increases the forcings by a few per cent.

Contents

1   Introduction

Greenhouse warming of Earth's surface and lower atmosphere is driven by *radiative forcing*, F, the difference between the flux of thermal radiant energy from a black surface through a hypothetical, transparent atmosphere, and the flux through an atmosphere with greenhouse gases, particulates and clouds, but with the same surface temperature[1]. Radiative forcing is often specified in units of watts per square meter (W m^{-2}). Forcing depends on the altitude, z, and on how the temperature and greenhouse-gas concentrations vary with altitude. The radiative heating rate, R, of the atmosphere is equal to the rate of change of the forcing with altitude, $R = dF/dz$, and can be specified in units of W m^{-2} km^{-1}. Over most of the atmosphere, $R < 0$, so thermal infrared radiation is a cooling mechanism that transfers absorbed solar energy back to space.

This paper has been written for readers with a strong background in quantitative sciences, who know little about radiation transfer in Earth's atmosphere. So we include material that is common knowledge to a small number of experts, but little known to the larger scientific community.
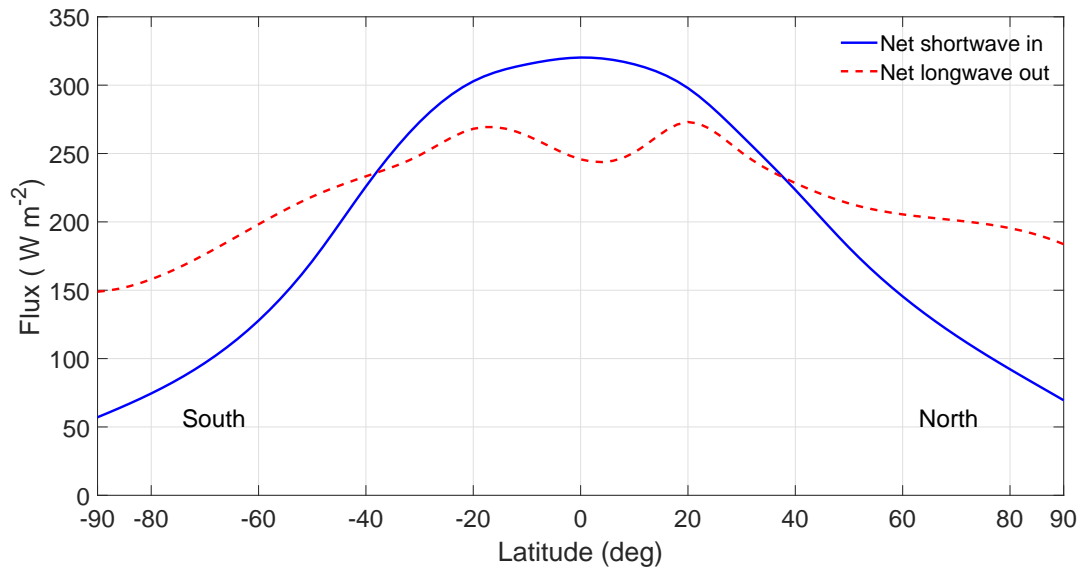

Figure 1: The continuous blue curve is the yearly average of incoming short-wave solar flux (net visible, near infrared and ultraviolet) absorbed by the Earth. The dashed red curve is the yearly average of the outgoing thermal flux (net longwave infrared) radiated to space by the Earth. Excess solar energy absorbed in the tropics is transported to the poles by mass flow in the atmosphere and oceans. The data is from satellite observations[2]. Adapted from PhysicalGeography.net [3].

Thermal radiation transfer in Earth's atmosphere has many similarities to that in stars, where methods for modeling radiation transfer were first developed [4]. But there are major differences. Because of the line structure of greenhouse gases, the opacity of Earth's atmosphere has a much more complicated dependence on frequency than that of stars. Over most of the volume of stars, radiative transfer is dominated by scattering in nearly fully-ionized

plasmas, with little absorption. In Earth's atmosphere, thermal radiation is absorbed by greenhouse gases, but scattering is negligible. Greenhouse molecules emit radiation at a temperature-dependent rate, whether they are absorbing radiation or not. Unlike the nearly isotropic heat flow from thermonuclear sources in the cores of stars, solar heating of the Earth is substantially stronger in the tropics than near the poles, as shown in Fig. 1. Meridional heat transport by the atmosphere and oceans, lets the poles emit more thermal energy to space than the solar energy they absorb. Tropical regions emit less than they absorb. Integrated over the surface of the Earth, the incoming shortwave radiation from the Sun is approximately equal to the outgoing longwave thermal radiation. But the surface-integrated fluxes of Fig. 1 are seldom exactly balanced. Changes of the average temperatures of the atmosphere and oceans, due to transient radiation imbalances, are small because of the huge thermal capacity of the oceans.

This paper is focussed on the dashed red curve of Fig. 1, the emission of thermal radiation to space. This is the aspect of radiation balance that is most directly affected by changes in the concentration of greenhouse gases. We discuss model atmospheres with average properties similar to that of Earth in the year 2019. We mainly consider "instantaneous" forcing changes that result when the concentration of one or more of the greenhouse gases changes, but all other atmospheric conditions remain fixed. Except for a brief discussion of temperature adjustments of the atmosphere to restore hypothetical radiation equilibrium[5], we do not discuss the many other feedbacks that contribute to the change of atmospheric properties. Important examples are changes in cloud cover and changes in the circulation patterns of the atmosphere and oceans. Discussions of these important topics can be found in papers by Schwartz[6, 7], Etminan *et al.*[8], Trenberth and Fasulo[9], Lindzen *et al.*[10], Myhre *al.*,[11, 12], Collins *et al.*[13], and Harde[14].

The concentrations of the major greenhouse gases are so large in the year 2019, that each gas interferes with its own radiative transfer and that of other greenhouse gases. The relative potencies of greenhouse gases are most clearly defined for a hypothetical, optically-thin limit, discussed in the final sections of this paper, when the radiative forcing of each greenhouse gas is proportional to its column density.

1.1 Altitude profiles

Radiation transfer in the cloud-free atmosphere of the Earth is controlled by only two factors: (1) the temperature $T = T(z)$ at the altitude z, and (2) the number densities, $N^{\{i\}} = N^{\{i\}}(z)$ of the ith type of molecule. Although the altitude profiles of temperature and number desities vary with latitude and longitude, the horizontal variation is normally small enough to neglect when calculating local radiative forcing.

Representative midlatitude altitude profiles of temperature [15], and greenhouse-gas concentrations[16], are shown in Fig. 2. Altitude profiles directly measured by radiosondes in ascending balloons [17] are always much more complicated than those of Fig. 2, which can be thought of as appropriate average profiles for the year 2019. The temperature profile was approximated with five altitude segments with constant temperature lapse rates, $-dT/dz = [\,6.5, 0, -1, -2.8, 2.145\,]$ K km^{-1}, between six altitude break points at $z = [\,0, 11, 20, 32, 47, 86\,]$ km.

On the left of Fig. 2 we have indicated the three most important atmospheric layers
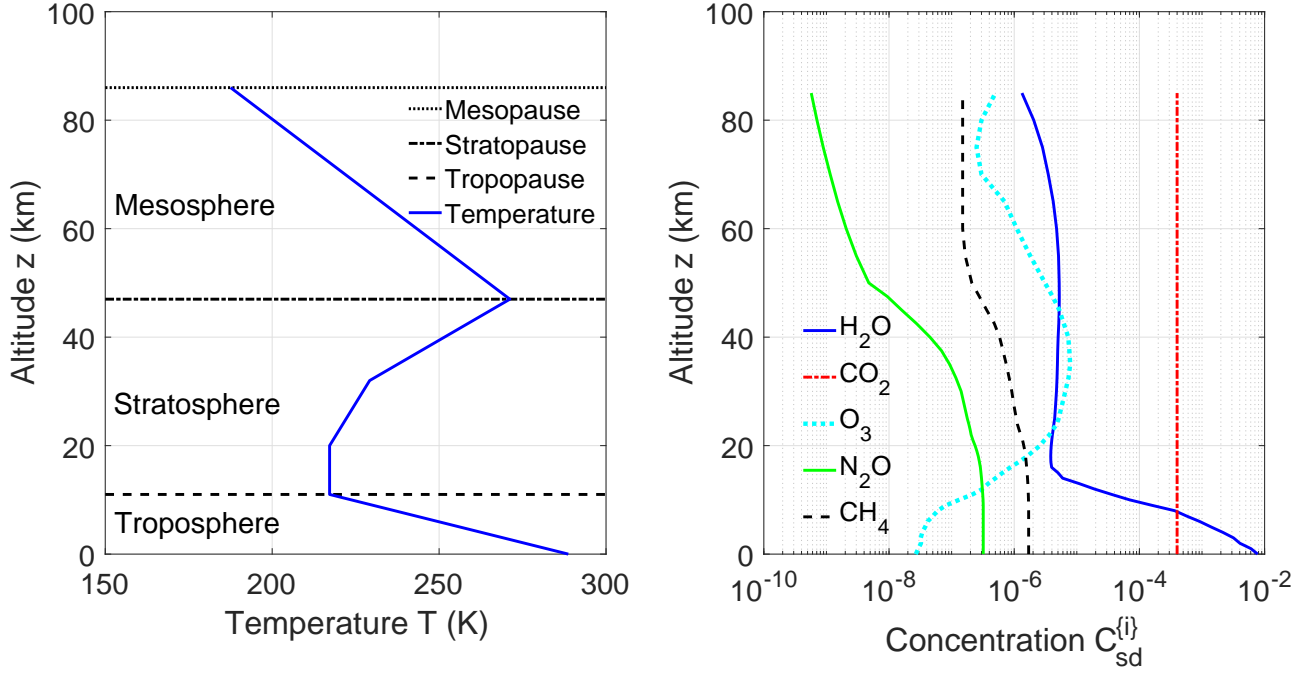
Figure 2: **Left.** A standard atmospheric temperature profile[15], $T = T(z)$. The Earth's mean surface temperature is $T(0) = 288.7$ K . **Right.** Standard concentrations[16], $C_{sd}^{\{i\}}$ of (3) for greenhouse molecules versus altitude z. At sea level the concentrations are 7750 ppm of H_2O, 1.8 ppm of CH_4 and 0.32 ppm of N_2O. The O_3 concentration peaks at 7.8 ppm at an altitude of 35 km, and the CO_2 concentration was approximated by 400 ppm at all altitudes.

for radiative heat transfer. The troposphere extends from the surface to the tropopause altitude, z_{tp}, which varies from about $z_{tp} = 18$ km at equatorial latitudes to about $z_{tp} = 8$ km at the poles. For midlatitudes, a representative tropopause altitude is $z_{tp} = 11$ km. The temperature T decreases with altitude in the troposphere. A representative lapse rate for midlatitudes is $-dT/dz = 6.5$ K km^{-1} as shown in Fig. 2. In the troposphere, convective transport of sensible heat and the latent heat of water vapor, especially near the equator, is as important as radiant heat transfer. Convecting parcels of air gain or lose little heat so their entropy changes only slightly with altitude. On average, the entropy increases fast enough with altitude to keep the troposphere buoyantly stable[18]. Air parcels that are displaced in altitude will oscillate up and down with periods of a few minutes. However, at any given time, large regions of the troposphere (particularly in the tropics) are unstable to moist convection. In these regions, the release of latent heat in deep convective clouds brings the vertical temperature profile close to that of a moist adiabat.

Above the troposphere is the stratosphere, which extends from the tropopause to the stratopause, at a typical altitude of $z_{sp} = 47$ km, as shown in Fig. 2. The temperature in the stratosphere is nearly constant at low altitudes, but it increases at higher altitudes due to the heating of ozone, O_3, molecules by ultraviolet sunlight. The stratosphere is much more stable to vertical displacements than the troposphere, and negligible moist convection

occurs there.

Above the stratosphere is the mesosphere, which extends from the stratopause to the mesopause at an altitude of about $z_{\text{mp}} = 86$ km. With increasing altitudes, radiative cooling, mainly by CO_2, becomes increasingly more important compared to heating by solar ultraviolet radiation. This causes the temperature to decrease with increasing altitude in the mesosphere.

Above the mesopause, is the extremely low-pressure thermosphere, where convective mixing processes are negligible. Temperatures increase rapidly with altitude in the thermosphre, to as high as 1000 K, due to heating by extreme ultraviolet sunlight, the solar wind and atmospheric waves. Polyatomic gases break up into individual atoms, and there is gravitational stratification, with lighter gases increasingly dominating at higher altitudes.

The vertical radiation flux Z, which is discussed below, can change rapidly in the troposphere and stratosphere. There can be a further small change of Z in the mesosphere. Changes in Z above the mesopause are small enough to be neglected, so we will often refer to the mesopause as "the top of the atmosphere" (TOA), with respect to radiation transfer.

Collision rates of molecules in the Earth's troposphere and stratosphere are sufficiently fast that a single local temperature $T = T(z)$ provides an excellent description of the distribution of molecules between translational, vibrational and rotational energy levels. The collision rates in the rarified upper mesosphere are slow enough that optical pumping and ionization of the D layer by solar radiation can produce small departures from local thermodynamic equilibrium (LTE)[19, 20]. But the departures have little effect on thermal radiation transfer and we will neglect them.

1.2   Naturally occurring greenhouse gases

We will model the atmosphere as a mixture of the molecules of Table 1. The mass of the ith type of molecule is

$$m^{\{i\}} = \frac{M^{\{i\}}}{n_{\text{A}}}. \tag{1}$$

where the molar masses, $M^{\{i\}}$, are summarized in Table 1, and Avogadro's number is $n_{\text{A}} = 6.022 \times 10^{23}$.

We denote the number density of the ith type of molecule by $N^{\{i\}}$. The total number density of molecules is

$$N = \sum_i N^{\{i\}}. \tag{2}$$

The concentrations $C^{\{i\}}$ of greenhouse gases are defined as

$$C^{\{i\}} = \frac{N^{\{i\}}}{N}, \quad \text{with} \quad \sum_i C^{\{i\}} = 1. \tag{3}$$

Standard concentrations, $C_{\text{sd}}^{\{i\}}$, based on observations[16], are shown as functions of altitude on the right of Fig. 2.

The total concentrations δC of greenhouse molecules, and $1 - \delta C$ of non-greenhouse molecules are

i	Molecule	$M^{\{i\}}$ (g)	$\hat{N}_{\text{sd}}^{\{i\}}$ (cm^{-2})
1	H_2O	18.05	4.67×10^{22}
2	CO_2	44.01	8.61×10^{21}
3	O_3	48.00	9.22×10^{18}
4	N_2O	44.01	6.61×10^{18}
5	CH_4	16.03	3.76×10^{19}
6	N_2	28.01	1.68×10^{25}
7	O_2	32.00	4.50×10^{24}
8	Ar	39.95	2.00×10^{23}

Table 1: Some properties of the most important atmospheric gases, listed in the second column. The molar masses, $M^{\{i\}}$, of (1) are listed in the third column. The fourth column lists the the standard column densities, $\hat{N}_{\text{sd}}^{\{i\}}$, defined by (11) for the standard altitude profiles of Fig. 2.

$$\sum_{i=1}^{5} C^{\{i\}} = \delta C, \quad \text{and} \quad \sum_{i=6}^{8} C^{\{i\}} = 1 - \delta C. \tag{4}$$

The mean mass m of an air molecule can be written as

$$\begin{aligned} m &= \sum_i m^{\{i\}} C^{\{i\}} \\ &= (\delta C) m^{\{g\}} + (1 - \delta C) m^{\{n\}}. \end{aligned} \tag{5}$$

The mean masses $m^{\{g\}}$ of greenhouse molecules, and $m^{\{n\}}$ of non-greenhouse molecules are

$$m^{\{g\}} = \sum_{i=1}^{5} \frac{m^{\{i\}} C^{\{i\}}}{\delta C} \quad \text{and} \quad m^{\{n\}} = \sum_{i=6}^{8} \frac{m^{\{i\}} C^{\{i\}}}{1 - \delta C} \tag{6}$$

Taking altitude-independent, standard values $C^{\{6\}}/(1-\delta C) = 0.7811$ for N_2, $C^{\{7\}}/(1-\delta C) = 0.2096$ for O_2, and $C^{\{8\}}/(1 - \delta C) = 0.0093$ for Ar, and using (6) with the molar masses of Table 1, the mean mass for non-greenhouse gases is found to be

$$m^{\{n\}} = 4.809 \times 10^{-23} \text{ g}. \tag{7}$$

For the standard concentrations of greenhouse gases shown in Fig. 2, the average mass (5) of an air molecule is a few parts per thousand lighter than $m^{\{n\}}$ at low altitudes, because relatively light H_2O molecules are the dominant admixture. Above the tropopause, the average mass m is about four parts in ten thousand heavier than $m^{\{n\}}$ because relatively heavy CO_2 molecules are the main admixture.

1.3 Pressure and number density

Air can be approximated as an ideal gas for which the pressure p is related to the number density N of (2) and the absolute temperature T by
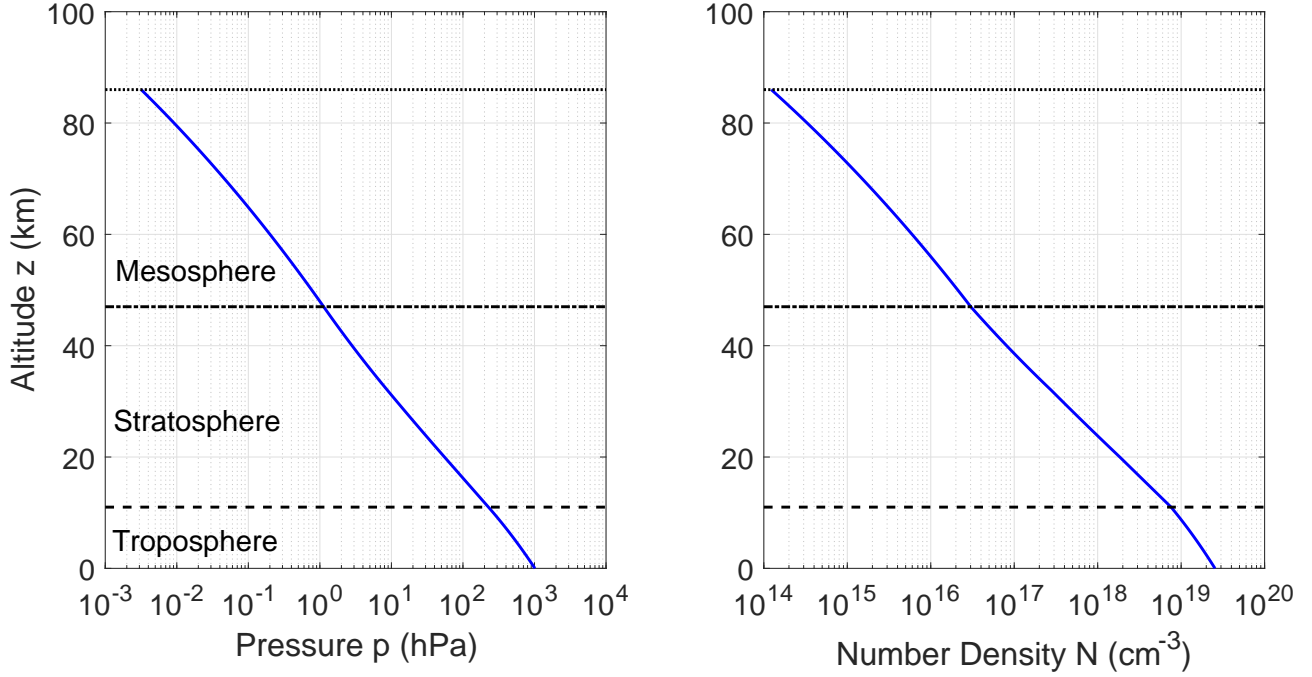
$$p = k_{\text{B}} N T. \tag{8}$$

Figure 3: **Left.** The pressure p of (10) at altitude z, corresponding to the temperature and concentrations of Fig. 2. The pressures in hPa at the surface, tropopause, stratopause and mesopause are approximately 1000, 200, 1 and 3×10^{-3} respectively. **Right.** The number density N according to the ideal gas law (8), for the profile of pressure p in the left panel, and for the profile of temperature T in Fig. 2.

Here Boltzmann's constant is $k_{\mathrm{B}} = 1.3806 \times 10^{-16}$ erg K^{-1}.

We consider an ideal, horizontally uniform atmosphere at rest in hydrostatic equilibrium. Then the infinitesimal drop in pressure, dp, over the increase in altitude from z to $z + dz$ is the weight per unit area of a slab of air of height dz, or

$$dp = -gmN dz = -\frac{gmp}{k_{\mathrm{B}}T} dz. \tag{9}$$

Here g is the downward acceleration of gravity at the altitude z. The atmosphere, with a scale height of order 10 km, is very thin compared to the Earth's radius, about 6370 km. So for discussions of most atmospheric properties, we will approximate the acceleration with the constant value $g = 981$ cm s^{-2}.

Integrating (9) we find the barometric equation for the pressure versus altitude

$$p = p_0 \exp\left(-\int_0^z \frac{gm'}{k_{\mathrm{B}}T'} dz' \right). \tag{10}$$

At the altitude z' the air temperature is T' and the mean mass of an air molecule is m'. Negligible loss in accuracy comes from replacing the altitude-dependent m' in (10) with the constant value $m^{\{n\}}$ of (7). The left panel of Fig. 3 shows the pressure p of (10) which

follows from the temperature profile of Fig. 2. The right panel of Fig. 3 shows the number density N that follows from p, T and the ideal gas law (8).

The number densities $N^{\{i\}} = C^{\{i\}} N$ depend strongly on the altitude z, both because of the variation of the concentrations, illustrated in Fig. 2 and because of the rapid decrease of number density N with altitude shown in Fig. 2. A simple measure of the quantity of greenhouse gas i, is the column density

$$\hat{N}^{\{i\}} = \int_0^{z_{\mathrm{mp}}} dz\, N^{\{i\}}. \tag{11}$$

The column densities of the most important atmospheric molecules, corresponding to the altitude profiles of Fig. 2, are shown in Table 1. The column densities are especially useful if the relative concentration profiles of Fig. 2 are independent of the column density. We will assume this to be the case in most subsequent discussions.

One can verify that the average weight per unit area of the atmospheric gases of Table 1 is the standard surface pressure,

$$p_0 = \frac{g}{n_{\mathrm{A}}} \sum_i M^{\{i\}} \hat{N}^{\{i\}} = 1.013 \text{ bar}. \tag{12}$$

The pressure unit is 1 bar $= 10^6$ dyne cm$^{-2} = 10^5$ Pa. Surface (sea-level equivalent) pressures of $p_0 = 0.90$ bar or less are occasionally recorded in tropical storms, and surface pressures as high as $p_0 = 1.08$ bar can occur during intense cold waves in Siberia.

1.4 Intensity and flux

The thermal-radiation power, d^3P, at the altitude z, that passes upward through a horizontal area increment dA, and propagates into a solid-angle increment $d\Omega$, in the frequency interval $d\nu$, is

$$d^3P = \tilde{I} \cos\theta\, dA\, d\Omega\, d\nu. \tag{13}$$

As sketched in Fig. 4, the direction of propagation, along the unit vector $\hat{\mathbf{n}}$, is specified by the colatitude (zenith) angle θ and the azimuthal angle ϕ. For downward radiation with $\theta > \pi/2$ the power increments are negative, $d^3P < 0$. Here $\tilde{I} = \tilde{I}(z, \nu, \theta)$ is the *spectral intensity*. Chandrasekhar[4] calls $\tilde{I}$ the *specific intensity*. The term *radiance* is also used in the climate literature[22]. The frequency of infrared radiation is usually specified by its spatial frequency, $\nu = 1/\lambda$, the inverse of the wavelength λ of the radiation, in units of cm^{-1}. The solid-angle increment is

$$d\Omega = d\phi \sin\theta d\theta = d\phi\, \varsigma^{-2} d\varsigma, \tag{14}$$

where the secant of the zenith angle is

$$\varsigma = \sec\theta. \tag{15}$$

The upward spectral flux[4], often called *irradiance* in the climate literature[22], is

$$\tilde{Z} = \int_{4\pi} d\Omega \left(\frac{d^3P}{dA\, d\Omega\, d\nu} \right) = \int_{4\pi} d\Omega \tilde{I} \cos\theta. \tag{16}$$
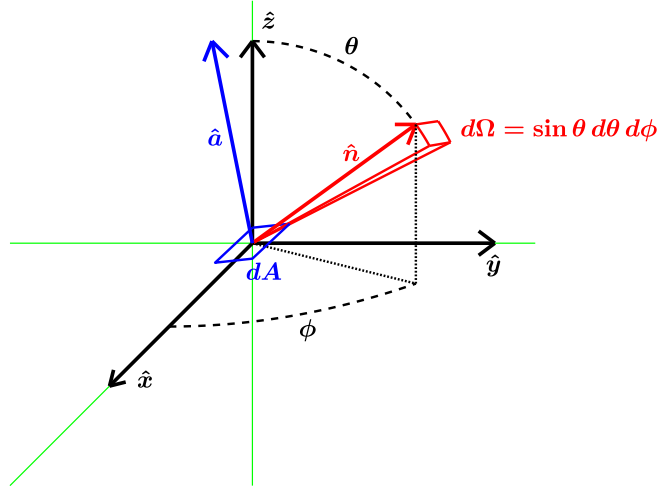
9

Figure 4: Coordinate system for radiation transfer, as discussed in (13) − (16). The unit vector along the direction of propagation, $\hat{\mathbf{n}}$, is related to the unit vectors $\hat{\mathbf{x}}$, $\hat{\mathbf{y}}$ and $\hat{\mathbf{z}}$ along the three Cartesian axes by $\hat{\mathbf{n}} = \hat{\mathbf{x}} \sin\theta \cos\phi + \hat{\mathbf{y}} \sin\theta \sin\phi + \hat{\mathbf{z}} \cos\theta$.

Let $\tilde{I}$ depend on θ, but not on the azimuthal angle ϕ. Then it is natural to write the upward spectral flux (16) as the difference between an upwelling part $\tilde{U}$ and a downwelling part $\tilde{D}$.

$$\tilde{Z} = \tilde{U} - \tilde{D}. \tag{17}$$

The upwelling is

$$\tilde{U} = \int_{\theta < \pi/2} d\Omega \, \cos\theta \, \tilde{I}(\theta) = 2\pi \int_1^\infty d\varsigma \, \varsigma^{-3} \tilde{I}, \tag{18}$$

where $\tilde{I} = \tilde{I}(\varsigma)$ and ς was given by (15). The downwelling is

$$\tilde{D} = -\int_{\theta > \pi/2} d\Omega \, \cos\theta \, \tilde{I}(\theta) = -2\pi \int_{-\infty}^{-1} d\varsigma \, \varsigma^{-3} \tilde{I}. \tag{19}$$

The terms upwelling and downwelling are widely used in the radiation-transfer literature to describe the angle-integrals (18) and (19).

The spectral intensity $\tilde{I}$ changes as light propagates through the atmosphere. Molecules in lower energy levels make transitions to upper levels, absorb radiation, and decrease the intensity. Molecules in upper levels make spontaneous or stimulated transitions to lower levels, emit radiation, and increase the intensity. The net attenuation coefficient $\kappa = \kappa(z, \nu)$ of radiation of frequency ν at altitude z is

$$\kappa = \sum_i N^{\{i\}} \sigma^{\{i\}}. \tag{20}$$

Here $\sigma^{\{i\}} = \sigma^{\{i\}}(z, \nu)$ is the absorption cross section of a molecule of type i for radiation of frequency ν at the altitude z. The cross section can depend strongly on altitude because the temperature and pressure depend on altitude. Temperature controls the distribution of the molecules between translational, rotational and vibrational states. Pressure, together with temperature, determines the width of the molecular resonance lines. We can use the attenuation coefficient (20) to define the vertical optical depth,

$$\tau = \int_0^z dz' \kappa', \tag{21}$$

where $\kappa' = \kappa(z', \nu)$. The optical depth (21) is the number of factors of e by which radiation of frequency ν would be attenuated if it propagated vertically upward from the surface at altitude $z = 0$ to an altitude z. The optical depth from the surface to top of the radiative atmosphere, the mesopause, is

$$\tau_{\mathrm{mp}} = \int_0^{z_{\mathrm{mp}}} dz' \kappa(z', \nu). \tag{22}$$

The optical depth τ is a more convenient variable than altitude z for calculations and discussions of radiation transfer.

In thermal equilibrium, the spectral intensity $\tilde{I}$ would be equal to the Planck brightness[4],

$$\tilde{B}(\nu, T) = \frac{2 h_{\mathrm{P}} c^2 \nu^3}{e^{\nu c h_{\mathrm{P}}/(k_{\mathrm{B}} T)} - 1}. \tag{23}$$

In (23) $h_P = 6.6261 \times 10^{-27}$ erg s is Planck's constant, and $c = 2.9979 \times 10^{10}$ cm s^{-1} is the speed of light.

If we approximate the solid Earth as a blackbody with a surface temperature T_0, we can let the spectral radiance at the surface be $\tilde{I}_0 = \tilde{B}_0$, where $\tilde{B}_0 = \tilde{B}(\nu, T_0)$ of (23). Since $\tilde{B}_0$ is independent of direction, (18) becomes

$$\tilde{U}_0 = 2\pi \tilde{B}_0 \int_1^\infty d\varsigma \, \varsigma^{-3} = \pi \tilde{B}_0. \tag{24}$$

The total upwelling, integrated over all frequencies is

$$U_0 = \int_0^\infty d\nu \, \tilde{U}_0 = \pi \int_0^\infty d\nu \, \tilde{B}_0 = \sigma_{\mathrm{SB}} T_0^4. \tag{25}$$

Using (23) in (25) gives the well-known formula[21] for the Stefan-Boltzmann constant in terms of other fundamental constants

$$\sigma_{\mathrm{SB}} = \frac{2\pi^5 k_{\mathrm{B}}^4}{15 h_{\mathrm{P}}^3 c^2}. \tag{26}$$

We will use the value $\sigma_{\mathrm{SB}} = 5.6704 \times 10^{-8}$ W m^{-2} K^{-4} is the Stefan-Boltzmann constant. We will not derive (26) here. Like Boltzmann and Stefan, take κ to be a quantity to be determined from experimental observations.

11

For cloud-free air, the intensity $\tilde{I}$ changes with optical depth as described by the Schwarzschild equation[4],

$$\frac{\partial \tilde{I}}{\partial \tau} = -\varsigma(\tilde{I} - \tilde{B}).$$
(27)

The Schwarzschild equation (27) is the scatter-free limit of a more general radiative-transfer equation[4] for molecules in thermodynamic equilibrium, and with significant scattering as well as absorption of radiation,

$$\frac{\partial \tilde{I}}{\partial \tau} = -\varsigma \left(\tilde{I} - [1 - \tilde{\omega}]\tilde{B} - \frac{\tilde{\omega}}{4\pi} \int_{4\pi} p(\hat{\mathbf{n}}, \hat{\mathbf{n}}')\tilde{I}' d\Omega' \right).$$
(28)

The spectral intensity $\tilde{I}$ of (28) is propagating along the unit vector $\hat{\mathbf{n}}$, which is specified by the angles θ and ϕ of Fig. 4. The probability that some of the intensity $\tilde{I}'$, propagating in the direction $\hat{\mathbf{n}}'$, is scattered into the direction $\hat{\mathbf{n}}$ is given by the phase function, $p(\hat{\mathbf{n}}, \hat{\mathbf{n}}') = p(\hat{\mathbf{n}}', \hat{\mathbf{n}})$, normalized such that

$$\int_{4\pi} p(\hat{\mathbf{n}}, \hat{\mathbf{n}}')d\Omega' = 4\pi.$$
(29)

For hypothetical isotropic scattering, the scattering phase function would be $p(\mathbf{n}, \mathbf{n}') = 1$. The single-scattering albedo of (28) is

$$\tilde{\omega} = \frac{\Gamma_r}{\Gamma_r + \Gamma_c}.$$
(30)

where Γ_r is the radiative energy loss rate of an excited greenhouse gas molecule, and Γ_c is the collisional loss rate. From Table 8 in the Appendix, we see that for all of the important natural greenhouse gases, the spontaneous radiation rates are relatively small, $\Gamma_r < 10^3$ s^{-1}. The collisional energy transfer rates, Γ_c, which are somewhat larger than gas-kinetic collision rates, are $\Gamma_c \sim 10^9$ s^{-1} at the surface, and $\Gamma_c \sim 10^6$ s^{-1} at the lower pressure of the stratopause. Therefore, the single-scattering albedo of (30) is very small, $\tilde{\omega} < 10^{-3}$, and it is an excellent approximation to set $\tilde{\omega} = 0$ in (28) to get (27).

Thermal radiation in Earth's atmosphere is almost never in thermal equilibrium, with $\tilde{I} = \tilde{B}$. If $\tilde{I} > \tilde{B}$ in (27), absorption exceeds spontaneous emission, heat is deposited in the molecules, and the intensity is attenuated. If $\tilde{I} < \tilde{B}$, spontaneous and stimulated emission exceed absorption, heat is extracted from the molecules and the intensity is amplified. An altitude interval dz corresponds to an interval $dl = dz\,\varsigma$ of propagation distance. So nearly horizontal rays with large secants, $|\varsigma| \gg 1$, approach the local Planck spectral intensity more rapidly than rays moving vertically upward or downward, which have $|\varsigma| = 1$. This is the reason for the "limb darkening" of the Sun[24].

The solution to (27) for upward intensity, with $\varsigma > 0$, can be written as the sum of a contribution $\tilde{I}_s$ of intensity emitted by the surface at altitude $z = 0$, and by a contribution $\tilde{I}_v$ of intensity emitted by greenhouse molecules in the volume of air between the surface and the observation altitude $z \geq 0$ where the optical depth is τ.

$$\tilde{I} = \tilde{I}_s + \tilde{I}_v.$$
(31)

The surface contribution is

$$\tilde{I}_s = e^{-\varsigma\tau}\tilde{B}_0$$
$$= \tilde{B}_0 - \varsigma \int_0^\tau d\tau' \tilde{B}_0 e^{-\varsigma(\tau-\tau')}. \tag{32}$$

The volume contribution is

$$\tilde{I}_v = \varsigma \int_0^\tau d\tau' \tilde{B}' e^{-\varsigma(\tau-\tau')}. \tag{33}$$

Here $\tilde{B}' = \tilde{B}(\nu, T')$, $T' = T(z')$ and $\tau' = \tau(z', \nu)$. The total spectral intensity of (31), $\tilde{I} = \tilde{I}(\theta)$ for upward intensity, with $\theta < \pi/2$ and $\varsigma \geq 1$, is therefore

$$\tilde{I} = \tilde{B}_0 + \varsigma \int_0^\tau d\tau' [\tilde{B}' - \tilde{B}_0] e^{-\varsigma(\tau-\tau')}. \tag{34}$$

According to (34), for an isothermal atmosphere with a temperature T' at altitude z' equal to the surface temperature T_0, and therefore with $\tilde{B}' = \tilde{B}_0$, the upward intensity $\tilde{I} = \tilde{I}(\theta)$ is equal to the Planck intensity, $\tilde{B}_0$ at the surface. The atmosphere is much like the "disappearing-filament" of optical pyrometers, designed to remotely measure temperatures of surfaces hot enough to emit visible radiation[25].

For downward radiation, with $\varsigma < 0$, the "surface radiation" is the microwave background radiation from outer space, which is very well-described as blackbody radiation[23]. Averaged over all incoming directions, the cosmic blackbody radiation has a temperature, $T_\infty = 2.725$ K, about a hundred times smaller than typical surface temperatures. According to (25), the flux from space will be approximately 10^8 times weaker than the flux from Earth's surface. Therefore, for downward radiation with $\varsigma < 0$, the intensity (31) is essentially all due to volume emission from greenhouse molecules above the observation altitude, and the analog of (34) is

$$\tilde{I} = -\varsigma \int_\tau^{\tau_{mp}} d\tau' \tilde{B}' e^{-\varsigma(\tau-\tau')}. \tag{35}$$

Substituting the expression (34) into (18) we find that the spectral upwelling is

$$\tilde{U} = \pi \tilde{B}_0 + 2\pi \int_0^\tau d\tau' E_2(\tau - \tau')[\tilde{B}' - \tilde{B}_0]. \tag{36}$$

Here $E_2(\tau)$ is an exponential integral. Exponential integrals occur naturally in the discussion of radiative transfer in planetary and stellar atmospheres, where they account for the slant paths of radiation between different altitudes. They can be defined (see Appendix 1 of Chandrasekhar[4] or **5.1.4** of Abramowitz[26]) by

$$E_n(\tau) = \int_1^\infty d\varsigma \, \varsigma^{-n} e^{-\varsigma\tau}. \tag{37}$$

Modern mathematical software packages often include the exponential integrals $E_1(x)$, along with other built-in functions like $\sin(x)$, $\ln(x)$, *etc.* The function $E_1(z) + \ln z$ has the power series,
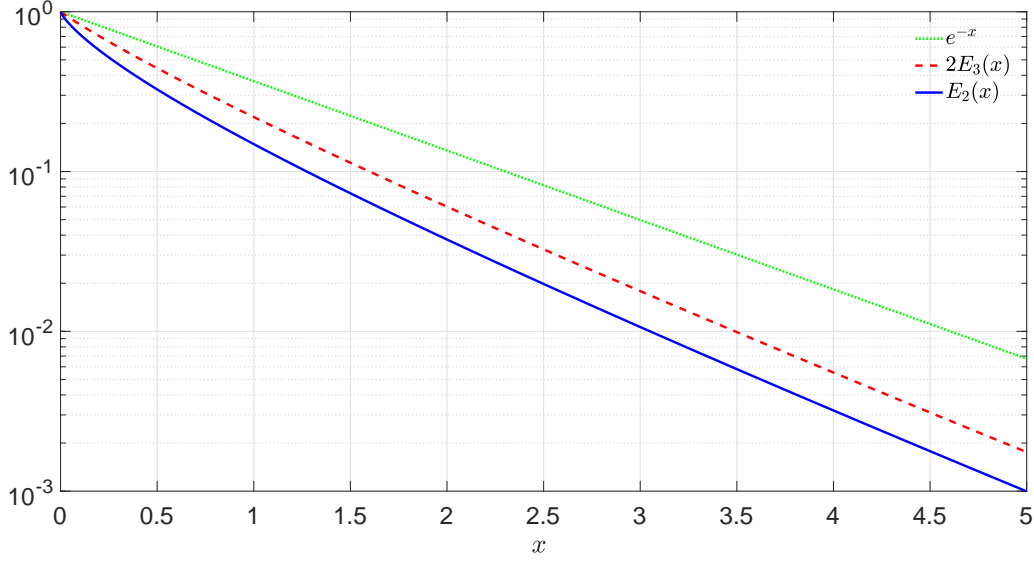
Figure 5: Attenuation functions for radiative transfer calculations. According to (32) and (33), for radiation propagating with a zenith angle, $\theta = \sec^{-1} \varsigma < \pi/2$, at an optical depth τ, the surface contribution to the intensity $\tilde{I}$ is attenuated by a factor $e^{-\varsigma\tau}$ and the contribution from greenhouse molecules at the optical depth τ' is attenuated by a factor $e^{-\varsigma(\tau-\tau')}$. According to (44) the surface contribution to the flux $\tilde{Z}$ is attenuated by a factor $2E_3(\tau)$ and the contributions from greenhouse-gas molecules, at optical depth τ', are attenuated by a factor $E_2(|\tau - \tau'|)$. The exponential integral functions $E_n(x)$ are defined by (37).

$$E_1(z) + \ln(z) = -\gamma - \sum_{n=1}^{\infty} \frac{(-z)^n}{n\,n!}, \tag{38}$$

that converges everywhere in the finite z plane. Here the Euler-Mascheroni constant is

$$\gamma = \lim_{n \to \infty} \left[\sum_{k=1}^{n} \frac{1}{k} - \ln(n) \right] = 0.57721\ldots \tag{39}$$

One can evaluate E_2, E_3, *etc.* from E_1 by repeated applications of the identity

$$n\,E_{n+1}(x) = e^{-x} - xE_n(x). \tag{40}$$

Integrating (37) by parts is one way to prove (40). Of particular interest are

$$E_2(x) \;=\; e^{-x} - x\,E_1(x), \tag{41}$$
$$2E_3(x) \;=\; (1-x)e^{-x} + x^2\,E_1(x). \tag{42}$$

Substituting (35) into (19) gives the downwelling spectral flux

$$\tilde{D} = 2\pi \int_{\tau}^{\tau_{\mathrm{mp}}} d\tau' E_2(\tau' - \tau)\tilde{B}'. \tag{43}$$

14

The net flux (17) is the difference between (36) and (43),

$$\tilde{Z} = 2\pi \tilde{B}_0 E_3(\tau) + 2\pi \int_0^\tau d\tau' E_2(\tau - \tau') \tilde{B}' - 2\pi \int_\tau^{\tau_{mp}} d\tau' E_2(\tau' - \tau) \tilde{B}'. \tag{44}$$

In using (36) to write (44) we noted that

$$
\begin{aligned}
\int_0^\tau d\tau' E_2(\tau - \tau') &= \int_0^\tau d\tau' E_2(\tau') \\
&= \int_0^\tau d\tau' \int_1^\infty d\varsigma\, \varsigma^{-2} e^{-\varsigma\tau'} \\
&= \int_1^\infty d\varsigma\, \varsigma^{-2} \left(\varsigma^{-1} - \varsigma^{-1} e^{-\varsigma\tau} \right) \\
&= \frac{1}{2} - E_3(\tau).
\end{aligned} \tag{45}
$$

The expression (44) has been known for a long time. For example, it can be found in the NASA reports by Yoshikawa[27] and Buglia[28]. The corresponding expression for an atmosphere where scattering cannot be neglected is more complicated and harder to solve.

The spectral forcing, $\tilde{F} = \tilde{F}(z, \nu)$, is defined as the difference between the spectral flux $\pi\tilde{B}_0 = \pi\tilde{B}(\nu, T_0)$ through a transparent atmosphere from a black surface with temperature T_0, and the spectral flux $\tilde{Z}$ of (44) for an atmosphere with greenhouse gases,

$$
\begin{aligned}
\tilde{F} &= \pi\tilde{B}_0 - \tilde{Z} \\
&= 2\pi \int_0^\tau d\tau' E_2(\tau - \tau')[\tilde{B}_0 - \tilde{B}'] + 2\pi \int_\tau^{\tau_{mp}} d\tau' E_2(\tau' - \tau) \tilde{B}'.
\end{aligned} \tag{46}
$$

If the spectral flux $\tilde{Z}$ decreases increases with altitude, energy is conserved by atmospheric heating or cooling. The spectral heating rate of atmospheric models is

$$\tilde{R} = -\frac{\partial \tilde{Z}}{\partial z} = \frac{\partial \tilde{F}}{\partial z}. \tag{47}$$

The frequency integrals of the flux (44) the forcing (46) and the heating rate (47) are

$$Z = \int_0^\infty d\nu\, \tilde{Z}, \tag{48}$$

$$F = \int_0^\infty d\nu\, \tilde{F} = \sigma_{SB} T_0^4 - Z, \tag{49}$$

$$R = \int_0^\infty d\nu\, \tilde{R} = -\frac{dZ}{dz} = \frac{dF}{dz}. \tag{50}$$

2 Line by Line Computations

The cross sections $\sigma^{\{i\}}$ of (20) are the sums of cross sections for all possible transitions from a lower level l of energy E_l and an upper level u of energy E_u of the same greenhouse molecule i. In this section, and subsequently, we will omit the superscript $\{i\}$ when it is clear from the

context that we are talking about a specific greenhouse molecule. Denote the Bohr (spatial) frequency ν_{ul} by

$$\nu_{ul} = \frac{E_{ul}}{h_{\mathrm{P}}c}, \quad \text{where} \quad E_{ul} = E_u - E_l. \tag{51}$$

The energy of a resonant photon is E_{ul}.

2.1 Cross sections

The cross section, $\sigma^{\{i\}} = \sigma$, for the ith type of greenhouse molecule is normally written as the sum of partial cross sections σ_{ul}, corresponding to each Bohr frequency ν_{ul},

$$\sigma = \sum_{ul} \sigma_{ul}. \tag{52}$$

The partial cross section, σ_{ul}, is assumed to be the product of a line-shape function, $G_{ul} = G_{ul}(\nu, \tau)$, and a line intensity, $S_{ul} = S_{ul}(T)$,

$$\sigma_{ul} = G_{ul}S_{ul}. \tag{53}$$

The line shape functions, G_{ul}, are normalized to have unit area,

$$\int_0^\infty G_{ul}d\nu = 1. \tag{54}$$

The units of G_{ul} are cm. The theoretical value for the line intensity is

$$S_{ul} = \eta_u \pi r_e f_{ul} W_l \left(1 - e^{-\nu_{ul}/\nu_T}\right) = \frac{\eta_u W_u \Gamma_{ul} E_{ul}}{4\pi \tilde{B}_{ul}}. \tag{55}$$

In (55), $r_e = e^2/(m_e c^2) = 2.818 \times 10^{-13}$ cm is the classical electron radius, where e is the elementary charge and m_e is the electron mass. The units of S_{ul} are cm. In (55) we designate the isotopologue fractions by $\eta_u = \eta_l$. The energy of a resonant photon is E_{ul}. Different isotopologues, for example ^{16}O ^{12}C ^{16}O and ^{16}O ^{13}C ^{16}O, will have different sets of Bohr frequencies ν_{ul}. The most abundant isotopologues for CO_2 are

$$\eta_{ul} = \begin{cases} 0.9843 & \text{for } ^{16}\text{O } ^{12}\text{C } ^{16}\text{O} \\ 0.0110 & \text{for } ^{16}\text{O } ^{13}\text{C } ^{16}\text{O} \\ 0.0040 & \text{for } ^{16}\text{O } ^{12}\text{C } ^{18}\text{O} \\ 0.0007 & \text{for } ^{16}\text{O } ^{12}\text{C } ^{17}\text{O}. \end{cases} \tag{56}$$

The last term of (55) contains the spectral intensity at the frequency ν_{ul},

$$\tilde{B}_{ul} = \tilde{B}(\nu_{ul}, T). \tag{57}$$

The probability W_n (with $n = u$ or $n = l$) to find a molecule in the vibration-rotation level n is

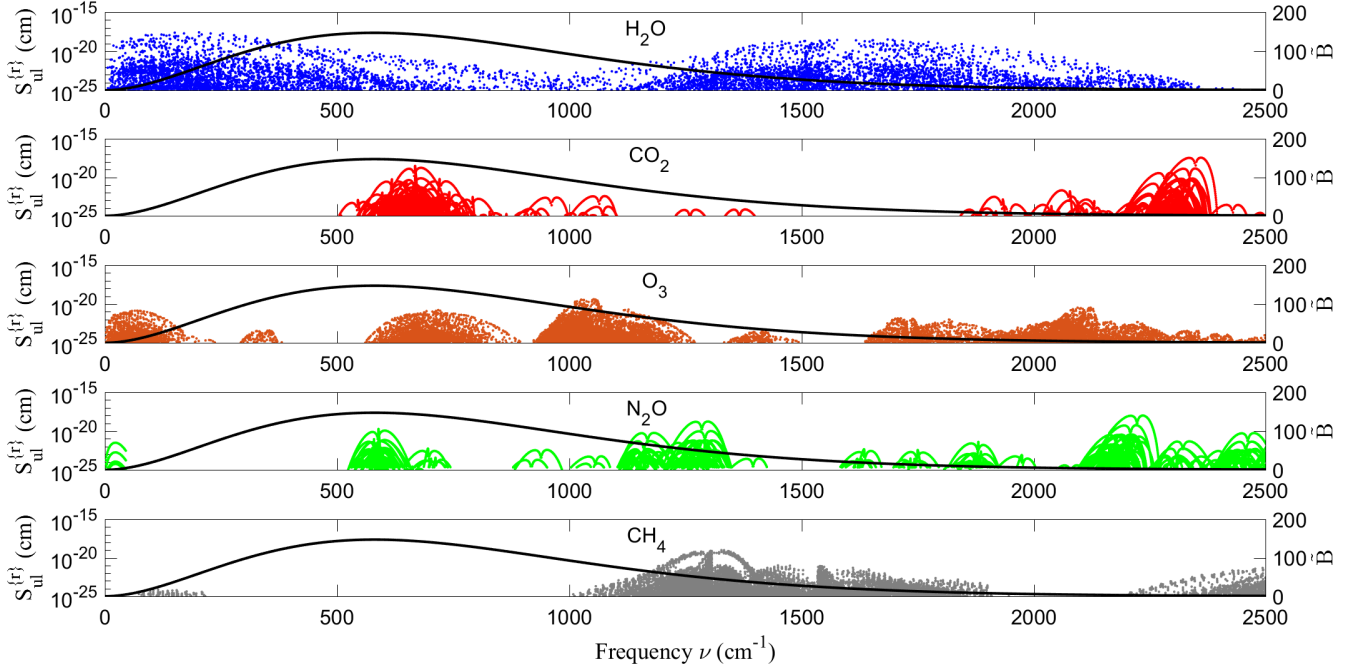$$W_n = \frac{g_n e^{-E_n/k_{\mathrm{B}}T}}{Q}. \tag{58}$$

16

Figure 6: Reference line intensities, $S_{ul}^{\{r\}}$ of (63) for the most important greenhouse gases, H_2O, CO_2, O_3, N_2O and CH_4 from the HITRAN data base [31]. The horizontal coordinate of each point represents the Bohr frequency ν_{ul} of a transition from an upper level u to a lower level l. The vertical coordinate of the point is the line intensity. For greater clarity we have plotted only 1/10, chosen at random, of the extremely large number of O_3 line intensities. The numbers of lines (in parenthesis) used for this work were: H_2O (31,112), CO_2 (20,569), O_3 (210,295), N_2O (43,152) and CH_4 (43,696). The smooth line is the Planck spectral intensity, $\tilde{B}$ of (23) in units of mW cm m^{-2} sr^{-1} for the HITRAN reference temperature, $T^{\{r\}} = 296$ K.

Here g_n is the statistical weight of the level n, the number of independent quantum states with the same energy E_n. For molecules in the level n, the statistical weight can be taken to be

$$g_n = (2j_n + 1)k_n, \tag{59}$$

where j_n is the rotational angular-momentum quantum number, and k_n is the nuclear degeneracy factor, that depends on the spins of the nuclei and whether they are identical or not. The partition function, $Q = Q(T)$, of the molecule is

$$Q = \sum_n g_n e^{-E_n/k_B T}. \tag{60}$$

The oscillator strength, f_{ul}, of (55) is related to the matrix elements of the electric dipole moment $\mathbf{M}$ of the molecule, between the upper-energy basis state $|j_u m_u\rangle$ with azimuthal

17

quantum number m_u and the lower-energy basis state $|j_l m_l\rangle$, by

$$f_{ul} = \frac{4\pi\nu_{ul}}{3g_l c\, r_e \hbar} \sum_{m_u m_l} \langle u\, m_u|\mathbf{M}|l\, m_l\rangle \cdot \langle l\, m_l|\mathbf{M}|u\, m_u\rangle. \tag{61}$$

The quantum numbers m_u label the various degenerate substates of the upper level u, and the m_l label the substates of the lower level l. If the levels are characterized by rotational quantum numbers j_u and j_l, the quantum numbers m_u and m_l can be thought of as the corresponding azimuthal quantum numbers, for example, $m_u = j_u, j_u - 1, \ldots, -j_u$.

The rate of spontaneous emission of photons when the molecule makes transitions from the upper level u to the lower level l is Γ_{ul}, the same as the Einstein A coefficient, $\Gamma_{ul} = A_{ul}$ [29, 30]. The spontaneous emission rate is related to the corresponding oscillator strength by

$$\Gamma_{ul} = \frac{8\pi^2 c\, r_e \nu_{ul}^2 f_{ul} g_l}{g_u}. \tag{62}$$

Theoretical molecular physics is not sufficiently well developed to use (61) to calculate oscillator strengths with the accuracy needed for radiation-transfer modelling. Instead, line intensities are determined from experimental measurements. Millions of molecular transitions that contribute to the infrared opacity of the atmosphere have been carefully measured, parameterized and archived in the HITRAN data base[31] .

From inspection of (55) we see that the line intensity $S_{ul} = S_{ul}(T)$ at some arbitrary temperature T is related to the intensity, $S_{ul}^{\{r\}} = S_{ul}(T_r)$ at a reference temperature $T^{\{r\}}$ where the partition function of (60) is $Q^{\{r\}} = Q(T^{\{r\}})$ by

$$S_{ul} = S_{ul}^{\{r\}} \frac{Q^{\{r\}}}{Q} \left(\frac{e^{-E_l/k_B T}}{e^{-E_l/k_B T^{\{r\}}}} \right) \left(\frac{1 - e^{-\nu_{ul}/\nu_T}}{1 - e^{-\nu_{ul}/\nu_{T^{\{r\}}}}} \right). \tag{63}$$

Data bases include line intensity values $S_{ul}^{\{r\}}$, Bohr frequencies ν_{ul}, lower-state energies E_l of all transitions, pressure-broadening coefficients, and other useful parameters. Fig. 6 shows some of the reference line intensities[31] used in this paper.

2.2 Line shapes

It is convenient to write the lineshape function as the product of a "core" profile $C_{ul} = C_{ul}(\nu)$ and a wing-suppression factor, $\chi_{ul} = \chi_{ul}(\nu)$,

$$G_{ul} = C_{ul}\chi_{ul}. \tag{64}$$

Core functions.   The core function is normally taken to be a Doppler-broadened Lorentzian, often called a Voigt profile[32]. The velocity v of the molecule toward the source of radiation shifts the resonant frequency (51) to $\nu_{ul}(1 + v/c)$. If we average over a Maxwellian distribution of velocities for molecules of mass m at the temperature T we find that a unit-area core function has the form

$$\begin{aligned}
C_{ul} &= \frac{\mu_{ul}}{\pi}\sqrt{\frac{m}{2\pi k_B T}} \int_{-\infty}^{\infty} \frac{e^{-mv^2/2k_B T}\, dv}{\mu_{ul}^2 + (\nu - \nu_{ul}[1 + v/c])^2} \\
&= \frac{\sqrt{\ln 2}}{\Delta\nu_{ul}\sqrt{\pi}} \Re[w(z_{ul})],
\end{aligned} \tag{65}$$

The half width at half maximum of a purely Doppler-broadened line is

$$\Delta\nu_{ul} = \nu_{ul}\sqrt{\frac{2k_B T \ln 2}{mc^2}} \approx 0.0005 \text{ cm}^{-1} \tag{66}$$

Here the representative Doppler half width, 0.0005 cm^{-1}, is for a resonance frequency ν_{ul} of the 667 cm^{-1} band of a CO_2 molecule near the cold mesopause.

The half-width at half maximum, μ_{ul}, of the Lorentzian function in the first line of (65) is almost entirely due to collisions. The contribution to μ_{ul} from spontaneous radiative decay, discussed in Appendix A, is negligible for altitudes below the mesopause. For the bending mode of CO_2, representative values[33] of μ_{ul} at atmospheric pressure p are

$$\mu_{ul} \approx 0.07\frac{p}{p_0} \text{ cm}^{-1}. \tag{67}$$

Here $p_0 = 1$ bar, the approximate atmospheric pressure at mean sea level. The pressure-broadening coefficients are often included in data bases. They depend somewhat on temperature and on the particular resonance, ul, involved.

For (65), a small, temperature-dependent pressure shift[33] must be added to the free-molecule Bohr frequency of (51), which we denote by $\nu_{ul}^{\{0\}}$, to define resonance frequency

$$\nu_{ul} = \nu_{ul}^{(0)} + \delta_{ul}\, p/p_0. \tag{68}$$

The magnitude of the pressure-shift coefficient δ_{ul}, which is sometimes tabulated in data bases, is of order

$$|\delta_{ul}| \approx 0.001 \text{ cm}^{-1}, \tag{69}$$

comparable to the Doppler half width (66). The small pressure shifts have negligible influence on radiative forcing calculations, but the pressure-broadening coefficients of (67) have a large effect on the transition of absorption lines from collision broadened in the troposphere and stratosphere, to Doppler broadened near the mesopause.

For the upper mesosphere, where the linewidth is dominated by Doppler broadening, it is convenient to use the Faddeeva function $w(z)$ [26], which is defined for arguments z in the upper half of the complex z plane ($\Im z \geq 0$), the only situation of interest to us, by

$$w(z) = \frac{1}{i\pi}\int_{-\infty}^{\infty}\frac{e^{-s^2}ds}{s-z}. \tag{70}$$

The integral extends along the real s axis. The argument z_{ul} of the Faddeeva function of (65) is the dimensionless complex number

$$z_{ul} = \frac{\sqrt{\ln 2}(\nu - \nu_{ul} + i\mu_{ul})}{\Delta\nu_{ul}}. \tag{71}$$

Fast and accurate computer algorithms [34] based on (70) have been developed to evaluate the Faddeeva functions $w(z)$ of (65) for any value of z_{ul}.

For most of the atmosphere, $|z_{ul}| \gg 1$, even at exact resonance when $z_{ul} = i\sqrt{\ln 2}\,\mu_{ul}/\Delta\nu_{ul}$. Under these conditions we can use the asymptotic expression

$$w(z) \sim \frac{i}{z\sqrt{\pi}} \quad \text{for} \quad |z| \geq 10. \tag{72}$$

19

and we can approximate the core function (65) with the Lorentzian profile

$$C_{ul} = \frac{\sqrt{\ln 2}}{\pi \Delta \nu_{ul}} \Re \left(\frac{i}{z_{ul}} \right) = \frac{\mu_{ul}/\pi}{\mu_{ul}^2 + (\nu - \nu_{ul})^2}. \tag{73}$$

For the very low pressures of the upper mesosphere, the parameter z_{ul} of (71) is nearly real, in the sense that $\Im(z_{ul}) \ll 1$. Under these conditions the real part of the Faddeeva function of (65) is very nearly $\Re[w(z_{ul})] = e^{-z_{ul}^2}$, and the core function (65) becomes the Gaussian profile

$$C_{ul} = \frac{\sqrt{\ln 2}}{\sqrt{\pi} \Delta \nu_{ul}} e^{-[\sqrt{\ln 2}(\nu - \nu_{ul})/\Delta \nu_{ul}]^2}. \tag{74}$$

Wing-suppression functions   Lorentz profiles like (73) give far too much absorption for large detunings $|\nu - \nu_{ul}|$, so it is necessary to include wing-suppression factors χ in the expression (64) for the lineshape function [35, 36]. Lorentzian line shapes come from assuming an infinitely short collision duration, but in fact collisions take a few ps for completion. The collisional interactions that lead to wing-suppression are not known well enough for reliable theoretical calculations, so we will use the empirical wing-suppression factor

$$\chi_{ul}(\nu) = \operatorname{sech}^2([\nu - \nu_{ul}]/\varpi). \tag{75}$$

Measurements on bands of CO_2, for example by Edwards and Strow [37], suggest that the far wings decrease approximately exponentially with detuning, $|\nu - \nu_{ul}|$, as does the wing-suppression function (75). We used the width parameter $\varpi = 2$ cm^{-1}, corresponding to a collision duration of a few picoseconds.

2.3   Numerical methods

The equations for radiation transfer, (34) or (44) are too complicated to be solved analytically, but they can be solved numerically. The basic steps we use are:

1. At a given frequency ν, cross sections σ of (52) are calculated as a function of altitude z. This is a time-consuming step since one must sum over the tens of thousands of contributions σ_{ul} of (53). One must evaluate temperature-dependent line intensities, S_{ul}, of (63) from the line intensities, $S_{ul}^{\{r\}}$ at the reference temperature T_r and from other parameters of the HITRAN data base[31]. A pressure-and-temperature-dependent lineshape function G_{ul} of (64) must also be evaluated. The cross sections σ_{ul} can vary by orders of magnitude with altitude z, because of the variation of temperature shown in Fig. 2 and the variation of pressure shown in Fig. 3.

2. The cross section $\sigma^{\{i\}}$ of the ith type of greenhouse gas, together with the altitude profiles $N^{\{i\}}$ of Fig. 2 are used to calculate the altitude-dependent attenuation rate κ of (20). It turns out that $\ln \kappa$ varies sufficiently smoothly in the 5 altitude segments of Fig. 2, that it is possible to use only 11 sampling altitudes, the 6 segment end points and the five midpoints, to accurately represent $\ln \kappa$, within the segment s as $\ln \kappa = a_{1s}z^2 + a_{2s}z + a_{3s}$. The 15 polynomial coefficients, a_{ks}, give an excellent parametrization of $\ln \kappa$ for each frequency ν.

3. The parameters a_{ks} obtained in the previous step are used to calculate sample attenuation coefficients, $\kappa_i = e^{\ln \kappa_i}$, at finely-spaced altitude samples, z_i, typically 100 samples for each segment of Fig. 2 or 501 altitude samples in total.

4. The κ_i are used to calculate sample optical depths τ_i from (21) and numerical integration, an example of which is shown in Fig. 7(b). Sample values $\tilde{B}_i$ of the Planck brightness of (23) also are calculated from sample temperatures T_i of Fig. 2, as shown in Fig. 7(a).

5. The convolutions (33) or (44) of the Planck brightness $\tilde{B}$ with the response functions $e^{-|\varsigma(\tau-\tau')|}$ or $E_2(|\tau - \tau'|)$, for $\tilde{I}$ and $\tilde{Z}$ respectively, are discretized, with appropriate account of the cusps at $|\tau - \tau'| = 0$.

6. The discrete convolutions are evaluated with the aid of fast Fourier transforms to get $\tilde{Z}_i$ at each of the 501 altitude samples, z_i, as shown in Fig. 7(c).

3   Intensity, Flux and Heating Rates

In this section we discuss model atmospheres with greenhouse-gas concentrations comparable to those of the year 2019. The spectral flux $\tilde{Z}$ of (44), the key descriptor of radiative-transfer, has a complicated dependence on frequency ν, on altitude z, on the altitude profiles of the temperature T and greenhouse gas concentrations $C^{\{i\}}$, and on latitude. We begin by discussing how $\tilde{Z}$ and related quantities depend on the altitude z.

3.1   Altitude dependence of $\tilde{B}$, $\tilde{Z}$ and $\tilde{R}$

According to (44), if we use the optical depth τ as a measure of altitude z, the Planck brightness $\tilde{B}$ serves as a source term for the flux $\tilde{Z}$, which consists of:

1. The surface blackbody flux, $\pi \tilde{B}_0$ for unit emissivity, attenuated by a factor $2E_3(\tau)$. The response function $2E_3(\tau)$, defined by (42), is sketched in Fig. 5.

2. Upwelling flux increments, $2\pi \tilde{B}' d\tau'$ emitted by molecules at lower altitudes between z' and $z' + dz'$, or between optical depths τ' and $\tau' + d\tau'$, are attenuated by a factor $E_2(\tau - \tau')$, defined by (41) and shown in Fig. 5.

3. Downwelling flux increments, $-2\pi \tilde{B}' d\tau'$ emitted by molecules at higher altitudes between z' and $z' + dz'$, or between optical depths τ' and $\tau' + d\tau'$, are attenuated by a factor $E_2(\tau' - \tau)$.

Most of the infrared radiation reaching the top of the atmosphere is emitted near an *emission height*, z_e, which is defined, for $\tau_{\mathrm{mp}} > \delta\tau_e$, by

$$\tau_{\mathrm{mp}}(\nu) - \tau(z_e, \nu) = \delta\tau_e, \tag{76}$$
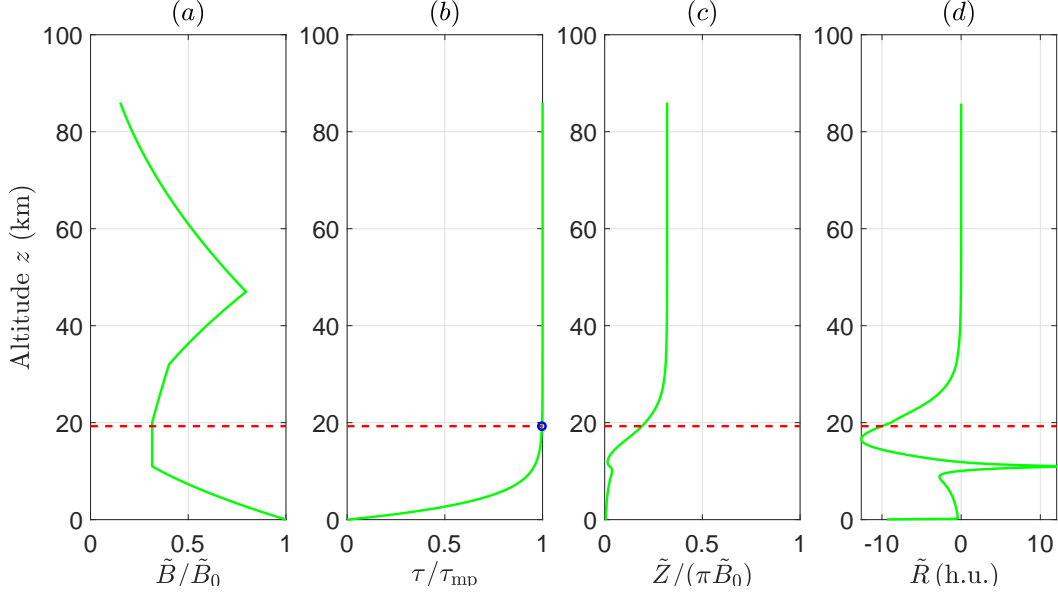
where

$$\delta\tau_e = 0.2674, \tag{77}$$

Figure 7: Altitude profiles for radiation of frequency $\nu = 690$ cm^{-1} of: (a) the Planck spectral brightness $\tilde{B}$ of (23) in units of the surface brightness, $\tilde{B}_0 = 129.6$ i.u. For brevity, we will occasionally use the spectral intensity unit, 1 i.u. $= 1$ mW m^{-2} cm sr^{-1} ; (b) the optical depth τ of (21) in units of the depth $\tau_{mp} = 83.1$ from the surface to the mesopause, the top of the radiative atmosphere: (c) the spectral flux $\tilde{Z}$ of (44) in units of $\pi\tilde{B}_0$; and (d) the spectral heating rate $\tilde{R}$ of (47). The spectral heating unit is 1 h.u. $= 1$ mW m^{-2} cm km^{-1}. The dashed red lines show the emission height $z_e = 19.3$ km of (76), where upwelling radiation of greenhouse gases is attenuated by a factor of $1/2$ before reaching the top of the atmosphere.

and where τ and τ_{mp} were defined by (21) and (22). For the optical depth increment $\delta\tau_e$ of (77) the attenuation function (41) for the flux from greenhouse gases has the value $E_2(\delta\tau_e) = 1/2$, so half of the radiation emitted by greenhouse gases at the emission height can escape to space.

For the standard atmosphere, the optical depths of (22) can be extremely large, $\tau_{mp} \gg \delta\tau_e$, at "blanket" frequencies ν near the centers of the absorption bands of greenhouse gases. For blanket frequencies the emissions heights z_e of (76) are at high altitudes. The extreme opposite of a blanket frequency is a "window" frequency, where there is little absorption by greenhouse gases, and $\tau_{mp} \leq \delta\tau_e$. For window frequencies, we can set $z_e = 0$, and assume that most radiation reaching space comes from the surface, with minor contributions from greenhouse gases.

As an illustrative example, Fig. 7(a) shows the altitude dependence of $\tilde{B}$, which is determined by the temperature $T = T(z)$ of Fig. 2 in accordance with (23). For all four panels the frequency is $\nu = 690$ cm^{-1}. The brightness $\tilde{B}$ decreases rapidly from the surface to the tropopause because of the drop in temperature. There is a secondary maximum of $\tilde{B}$ at the stratopause, the altitude of maximum heating of O_3 by solar ultraviolet radiation.

Fig. 7(b) shows how the optical depth τ depends on the altitude z in accordance with (21). The total optical depth from the surface to the mesopause is $\tau_{mp} = 83.1$. At the
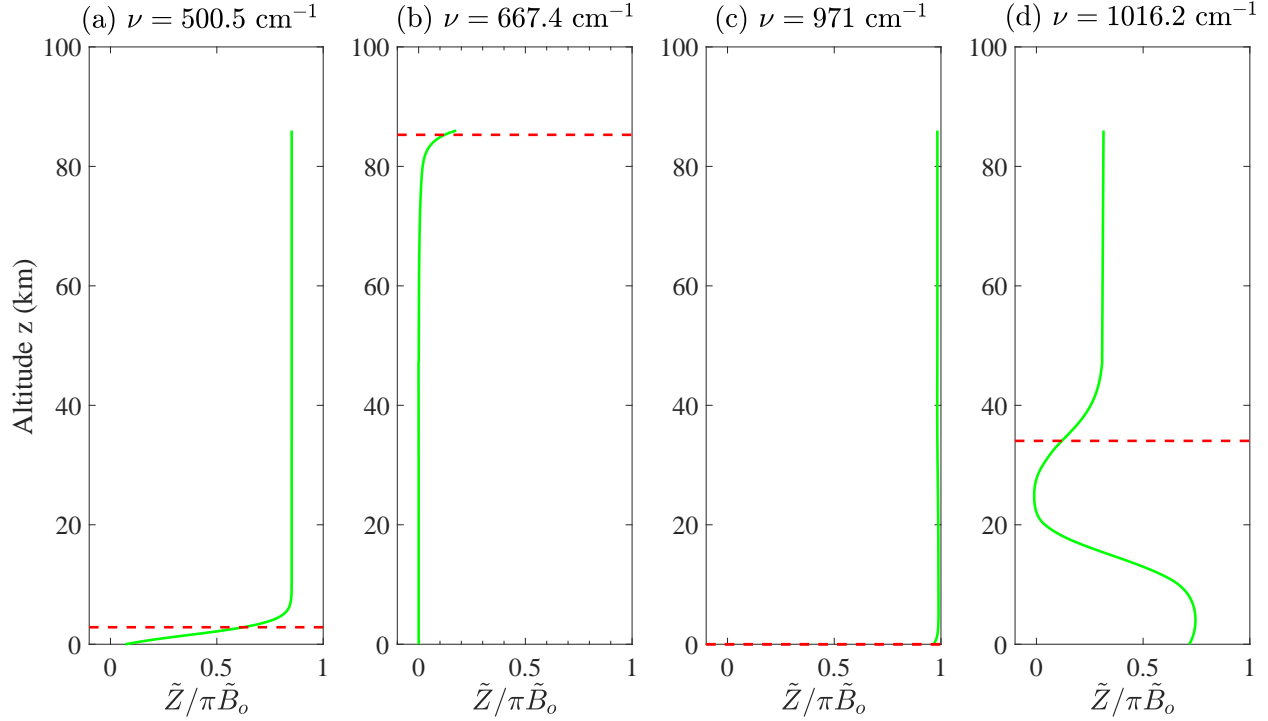
22

Figure 8: Spectral fluxes $\tilde{Z}$, like those of Fig. 7, for other representative frequencies, ν : (a) $\tau_{\mathrm{mp}} = 2.30$, $z_e = 2.9$ km, $\tilde{B}_o = 134.2$ i.u.; (b) $\tau_{\mathrm{mp}} = 51687$, $z_e = 85.3$ km, $\tilde{B}_o = 131.8$ i.u.; (c) $\tau_{\mathrm{mp}} = 0.016$, $z_e = 0$ km, $\tilde{B}_o = 86.4$ i.u.; (d) $\tau_{\mathrm{mp}} = 7.11$, $z_e = 34.0$ km, $\tilde{B}_o = 79.3$ i.u.. Here the spectral intensity unit is 1 i.u. $= 1$ mW m^{-2} cm sr^{-1}.

emission height, $z_e = 19.3$ km, the optical depth is $\tau = \tau_{\mathrm{mp}} - \delta\tau_e = 82.8$, or $\tau/\tau_{\mathrm{mp}} = 0.996$, as marked by the blue circle.

Fig. 7(c) shows the altitude dependence of the spectral flux $\tilde{Z}$ of (44). Near the surface, the upwelling spectral flux, $\pi\tilde{B}_0 = 407$ mW m^{-2} cm is nearly canceled by almost equal and opposite downwelling flux from greenhouse gases in the atmosphere above. The spectral flux increases modestly with altitude in the troposphere, and it reaches a maximum at the tropopause at $z = 11$ km. $\tilde{Z}$ drops to nearly zero from 11 km to 15 km. From about 15 km to 30 km, altitudes near the emission height $z_e = 19.3$ km, the flux $\tilde{Z}$ increases rapidly to its asymptotic value in the higher atmosphere.

Fig. 7(d) shows the altitude dependence of the spectral heating rate, $\tilde{R}$, of (47). At most altitudes in the troposphere , $\tilde{R} < 0$, which means that radiation at the frequency $\nu = 690$ cm^{-1} is being amplified in the troposphere at the expense of heat extracted from greenhouse-gas molecules. There is a narrow spike of heating around the tropopause. The cooling rate, $-\tilde{R}$, maximizes near the emission height $z_e = 19.3$ km, where the upwelling radiation of greenhouse molecules is attenuated by a factor of $1/2$.

The altitude profiles of $\tilde{Z}$ for a few other representative frequencies are shown in Fig. 8. Fig. 8(a) shows a moderate blanket frequency $\nu = 500.5$ cm^{-1}, where the optical depth, $\tau_{\mathrm{mp}} = 2.30$, is moderately larger than the emission depth, $\delta\tau_e = 0.2673$, of (76). The emission height $z_e = 2.9$ km is in the lower troposphere. From inspection of Fig. 6, we see

that transitions of the pure rotation spectrum of H_2O dominate the atmospheric opacity at the frequency, $\nu = 500.5$ cm^{-1}.

Fig. 8(b) shows an extreme blanket frequency, with an optical depth $\tau_{mp} = 51,687$, and an emission height $z_e = 85.3$ km, just below the mesopause. As one can see in Fig. 9, the opacity at the frequency, $\nu = 667.4$ cm^{-1}, is mostly due to a Q-branch vibration-rotation transition of CO_2, with rotational angular momentum $j = 4$ in the initial and final states. The intense cooling rate, $-\tilde{R} = \partial \tilde{Z}/\partial z$, near the top of the atmosphere helps to drive down the temperature of the mesopause.

Fig. 8(c) shows an extreme window frequency, $\nu = 971$ cm^{-1}, where the optical depth is only $\tau_{mp} = 0.016$. At this frequency, and in the absence of clouds, surface radiation reaches space with negligible attenuation by greenhouse gases. One of the infrared images of the Earth's disk, provided by geosynchronous satellites[39], is in a band centered on the wavelengh $\lambda = 1/(971$ cm$^{-1}) = 10.3\,\mu$m, the "clean infrared window."

Fig. 8(d) shows a blanket frequency, $\nu = 1016.2$ cm^{-1}, with a moderate optical depth $\tau_{mp} = 7.11$ in the O_3 band. Not surprisingly, the emission height, $z_e = 34$ km is in the upper stratosphere, where Fig. 2 shows that the O_3 concentration maximizes and heating by ultraviolet sunlight keeps the temperature higher than in the lower stratosphere. Downward spectral flux from the emission height contributes to pronounced spectral heating of the lower stratosphere. This is in contrast to the radiative cooling that characterizes most frequencies and most altitudes.

3.2   Frequency dependence of $\tilde{Z}$ and $\tilde{I}$

Fig. 9 shows the spectral flux, $\tilde{Z}$, and π times the vertical spectral intensity, $\tilde{I}$, for $\theta = 0$. These were calculated at the mesopause altitude $z_{mp} = 86$ km, the top of the radiative atmosphere, with (44) and (34), for frequencies from 667.3 cm^{-1} to 667.5 cm^{-1}, where most of the absorption is due to CO_2 molecules.

The five prominent resonances of Fig. 9 are Q-branch absorption lines of the most abundant isotopologue, $^{16}O^{12}C^{16}O$, near the mesopause, where the pressure is low enough that Doppler broadening (66) determines the line width. The rotational quantum numbers j for $\Delta j = 0$ transitions from lower vibrational states of the bending mode and upper states with one unit of vibrational excitation, are $j = 2, 4, 6, \ldots$. Odd values of j are forbidden because of the identical ^{16}O atoms with nuclear spin $I = 0$. The resonances are thermal-infrared analogs of the Fraunhofer dark lines of the sun [38]. The resolution of most satellite spectrometers is far too coarse to resolve these Q absorption lines.

For frequencies between the Q resonances, most of the flux and intensity is from near the stratopause at an altitude of $z_{sp} = 47$ km, where there is a temperature maximum $T(z) = 271.2$ K, as can be seen from Fig. 2. The very weak fluxes for frequencies near the minima of the narrow Q lines are from molecules near the mesopause, at an altitude of 86 km, where the temperature reaches its minimum value of 187.5 K. An example is shown in Fig. 8(b).

The dashed red line shows the flux, $\pi \tilde{B}$, of a blackbody at the temperature of $T = 288.7$ K of the surface. This is the flux that would be observed at the top of a hypothetical atmosphere with no greenhouse gases.

A spectrometer in a satellite can measure the upward spectral intensity $\tilde{I}(\theta)$ of (34) at
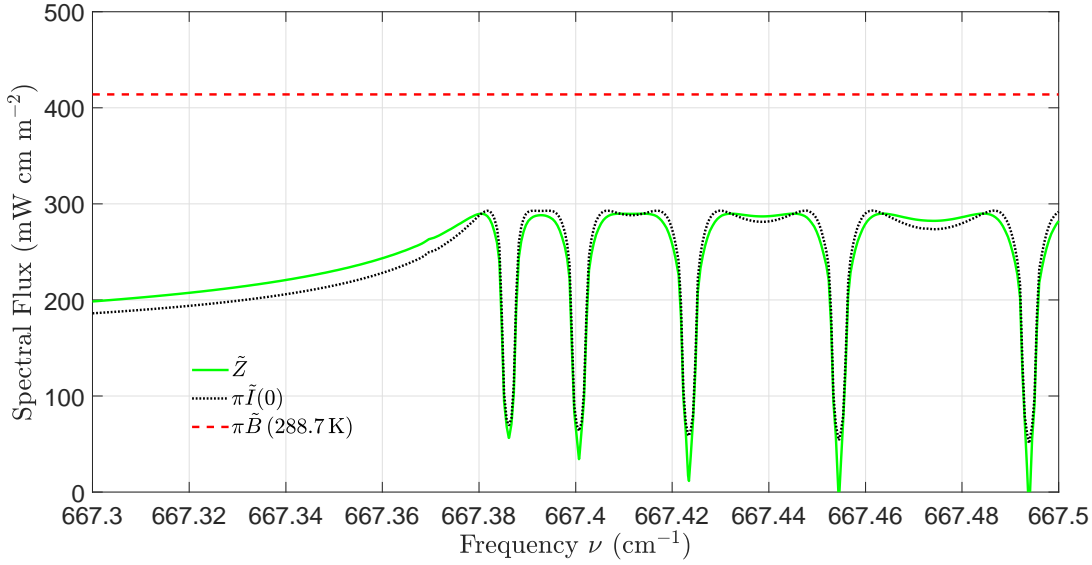
Figure 9: Mesopause ($z_{\mathrm{mp}} = 86$ km) values of the spectral flux $\tilde{Z}$ of (36) and of $\pi\tilde{I}(\theta)$, the upward intensity (34) with $\theta = 0$ and $\varsigma = \sec\theta = 1$. If the intensity $\tilde{I}(\theta)$ were independent of the angle θ, the two curves would be identical. Most of the flux is from CO_2 molecules in the stratosphere and mesosphere at emission heights z_e given by (76). The dashed red curve is the flux for a transparent atmosphere if the surface temperature is $T_0 = 288.7$ K.

the top of the atmosphere for radiation in a narrow solid-angle increment, $d\Omega$, making an angle θ with the vertical, as sketched in Fig. 4. In analogy to (24), if $\tilde{I}(\theta)$ were independent of θ we would have $\tilde{Z} = \pi\tilde{I}(0)$. But as shown in Fig. 9, $\pi\tilde{I}(0)$ and $\tilde{Z}$ differ by a few per cent because the intensity $\tilde{I}(\theta)$ does depend on θ.

For radiation frequencies near the centers of the strong Q lines, the absorption cross section σ is so large that only CO_2 molecules close to the top of the atmosphere can contribute to $\tilde{I}$ or $\tilde{Z}$, as illustrated in Fig. 8(b). Intensities, $\tilde{I}(\theta)$, with more slanted paths, $\theta > 0$ will be weaker than the intensity $\tilde{I}(0)$ of vertical paths, with $\theta = 0$, since vertical paths have more contributions from molecules in the deeper, warmer mesosphere. There is "limb darkening," like that of the visible spectral intensity of the Sun[24], and $\tilde{Z} < \pi\tilde{I}(0)$.

At the lowest frequency displayed in Fig. 9, the attenuation is small enough that the vertical intensity comes from the cold lower stratosphere. Then slant paths with $\theta > 0$ allow more CO_2 molecules near the warm stratopause to contribute to $\tilde{I}(\theta)$. There is "limb brightening," for moderately positive values of θ, and $\tilde{Z} > \pi\tilde{I}(0)$.

As one can see from Fig. 9, to accurately model the frequency dependence of $\tilde{Z}$ or $\tilde{I}$ one needs several frequency samples per Doppler half-width (66) or about 1 frequency sample per 0.0001 cm^{-1}. But such extremely high resolution is not needed to calculate the frequency-integrated forcings F of (49). We have found empirically that frequency sampling intervals of $\delta\nu = 0.1$ cm^{-1} are adequate to give values of $\langle\tilde{F}\rangle$ from (78), that are within about 0.1% of the values obtained with $\delta\nu = 0.0001$ cm^{-1}. Using a resolution of 0.1 cm^{-1} instead of 0.0001 cm^{-1} speeds up the calculation by a factor of 1000, which allows one to use laptop computers for the computations illustrated in this paper.
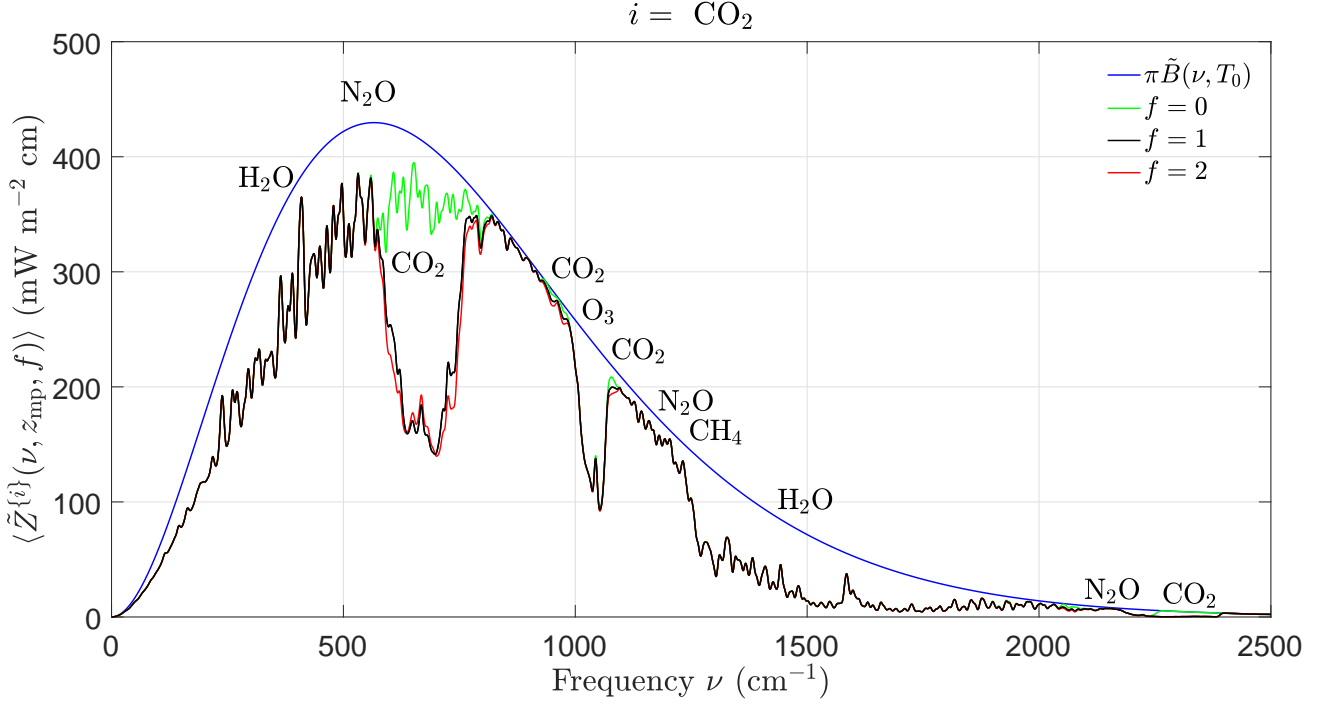
Figure 10: Effects of changing concentrations of carbon dioxide, CO_2 on the filtered spectral flux $\langle \tilde{Z}^{\{i\}}(\nu, z_{\mathrm{mp}}, f) \rangle$ of (82) at the mesopause altitude, $z_{\mathrm{mp}} = 86$ km. The width of the filter (81) was $\Delta\nu = 3$ cm^{-1}. The smooth blue line is the spectral flux, $\tilde{Z} = \pi\tilde{B}(\nu, T_0)$ from a surface at the temperature $T_0 = 288.7$ K for a transparent atmosphere with no greenhouse gases. The green line is $\langle \tilde{Z}^{\{i\}}(\nu, z_{\mathrm{mp}}, 0) \rangle$ with the CO_2 removed but with all the other greenhouse gases at their standard concentrations. The black line is $\langle \tilde{Z}^{\{i\}}(\nu, z_{\mathrm{mp}}, 1) \rangle$ with all greenhouse gases at their standard concentrations. The red line is $\langle \tilde{Z}^{\{i\}}(\nu, z_{\mathrm{mp}}, 2) \rangle$ for twice the standard concentration of CO_2 but with all the other greenhouse gases at their standard concentrations. Doubling the standard concentration of CO_2 (from 400 to 800 ppm) would only cause a forcing increase (the area between the black and red lines) of $\Delta F^{\{i\}} = 3.0$ W m^{-2}, as shown in Table 2.

3.3 Filtered spectral flux, $\langle \tilde{Z} \rangle$

High resolution spectrometers on satellites seldom provide measurements of intensity $\tilde{I}$ with resolutions less than 1 cm^{-1}, but still much coarser than the resolution of the model calculation of Fig. 9 . For comparison of modeled spectral quantities $\tilde{X}$ (e.g. $\tilde{I}, \tilde{Z}, \tilde{F}, \tilde{R}$) with observations, or simply for convenience in plotting graphs, it is useful to use the filtered spectral quantities,

$$\langle \tilde{X} \rangle(z, \nu) = \int_0^\infty d\nu' J(\nu, \nu') \tilde{X}(z, \nu'). \tag{78}$$

The filter function $J(\nu, \nu')$ is designed to smooth out sharp changes with frequency. It is normalized so that
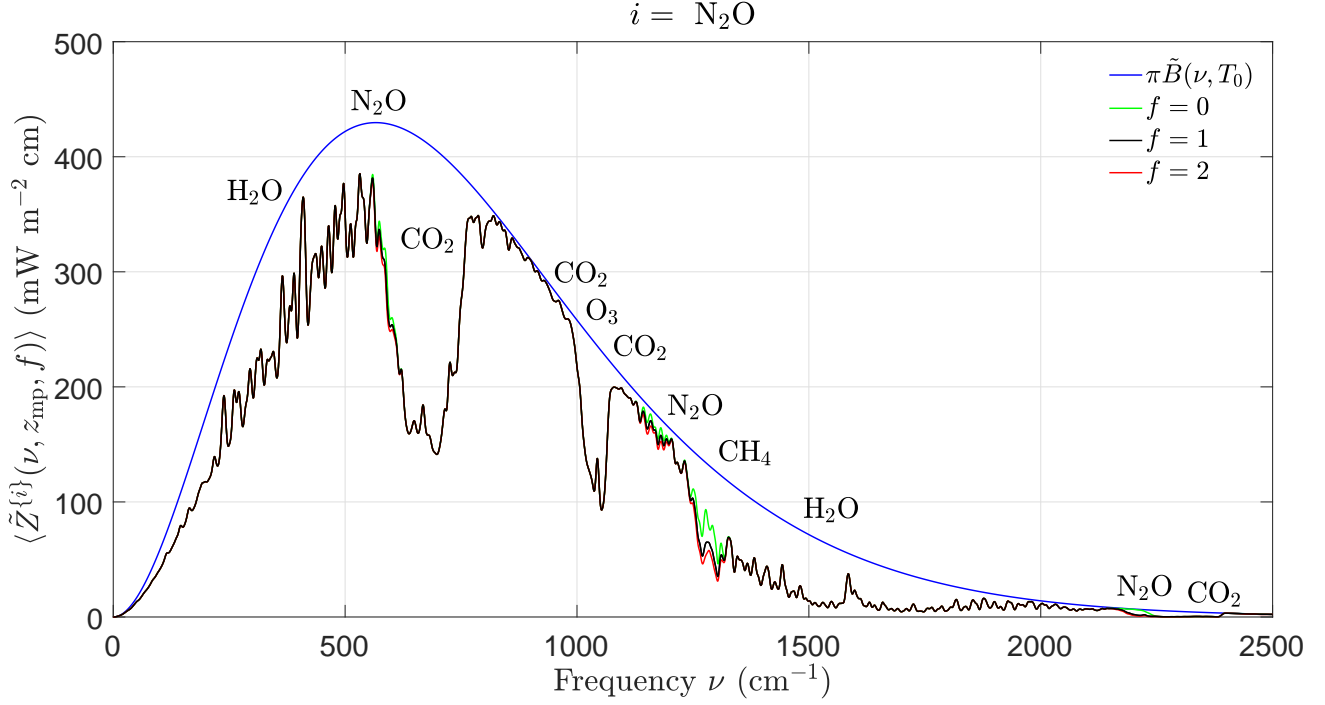
$$\int_{-\infty}^\infty d\nu J(\nu, \nu') = 1. \tag{79}$$

Figure 11: Effects of changing concentrations of nitrous oxide, N_2O, on the filtered spectral flux $\langle \tilde{Z}^{\{i\}}(\nu, z_{mp}, f)\rangle$ of (82) at the mesopause altitude, $z_{mp} = 86$ km. The blue and black lines have the same meanings as for Fig. 10. The green line is $\langle \tilde{Z}^{\{i\}}(\nu, z_{mp}, 0)\rangle$ with the N_2O removed but with all the other greenhouse gases at their standard concentrations. The red line is $\langle \tilde{Z}^{\{i\}}(\nu, z_{mp}, 2)\rangle$ with twice the standard concentration of N_2O but with all the other greenhouse gases at their standard concentrations. Doubling the standard concentration of N_2O would only cause a forcing increase (the area between the black and red lines) of $\Delta F^{\{i\}} = 1.1$ W m^{-2}, as shown in Table 2.

From (78) and (79) we see that the unfiltered spectral flux $\tilde{Z}$ and filtered spectral flux $\langle \tilde{Z}\rangle$ have the same frequency integral

$$Z = \int_0^\infty d\nu \tilde{Z} = \int_0^\infty d\nu \langle \tilde{Z}\rangle, \tag{80}$$

and represent the same total flux Z.

We found it convenient to use Gaussian filter functions with a width parameter $\Delta\nu$,

$$J(\nu, \nu') = \frac{e^{-(\nu-\nu')^2/2\Delta\nu^2}}{\sqrt{2\pi}\Delta\nu}. \tag{81}$$

The effects on radiative transfer of changing the column density of the ith greenhouse gas to some multiple f of the standard value, $\hat{N}_{sd}^{\{i\}}$, can be displayed with filtered spectral fluxes

$$\langle \tilde{Z}^{\{i\}}(\nu, z, f)\rangle = \langle \tilde{Z}(\nu, z, \hat{N}_{sd}^{\{1\}}, \ldots, \hat{N}_{sd}^{\{i-1\}}, f\hat{N}_{sd}^{\{i\}}, \hat{N}_{sd}^{\{i+1\}}, \ldots, \hat{N}_{sd}^{\{n\}})\rangle. \tag{82}$$
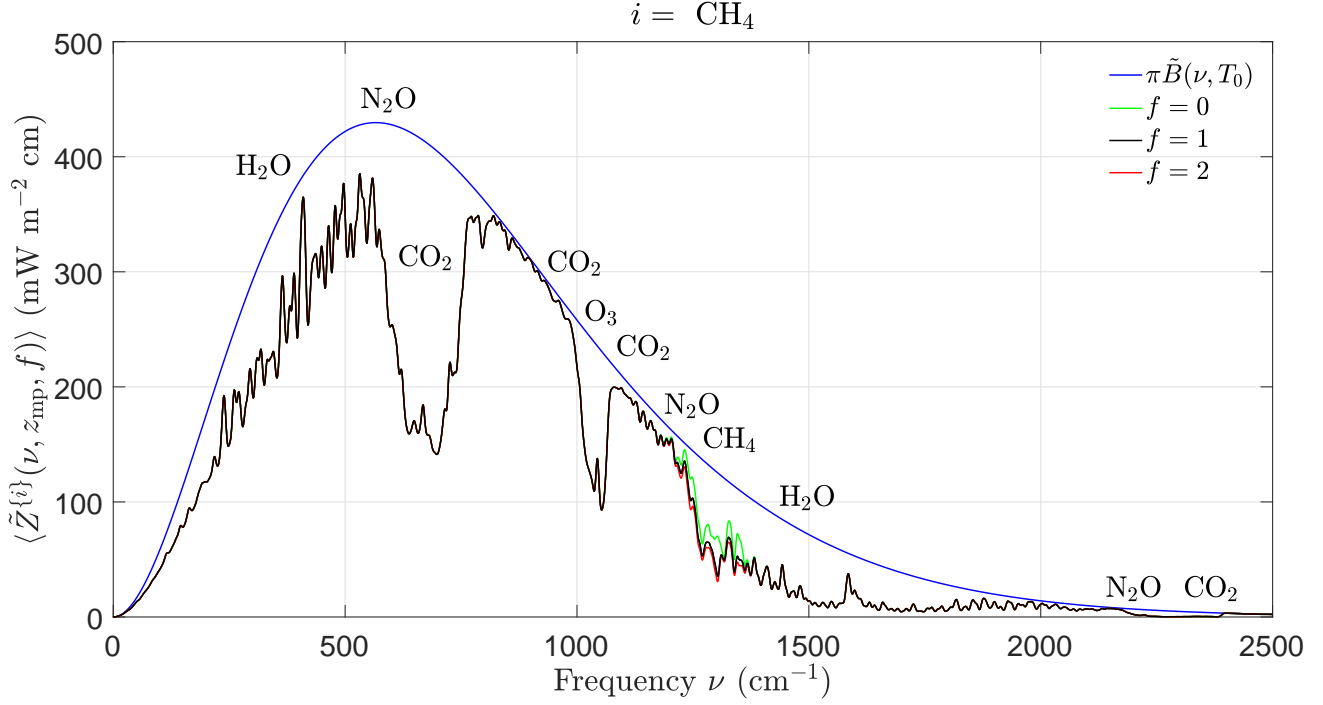
Figure 12: Effects of changing concentrations of methane, CH_4, on the filtered spectral flux $\langle \tilde{Z}^{\{i\}}(\nu, z_{mp}, f)\rangle$ of (82) at the mesopause altitude, $z_{mp} = 86$ km. The blue and black lines have the same meanings as for Fig. 10. The green line is $\langle \tilde{Z}^{\{i\}}(\nu, z_{mp}, 0)\rangle$ with the CH_4 removed but with all the other greenhouse gases at their standard concentrations. The red line is $\langle \tilde{Z}^{\{i\}}(\nu, z_{mp}, 2)\rangle$ with twice the standard concentration of CH_4 but with all the other greenhouse gases at their standard concentrations. Doubling the standard concentration of CH_4 would only cause a forcing increase (the area between the black and red lines) of $\Delta F^{\{i\}} = 0.7$ W m^{-2}, as shown in Table 2.

Figures 10 – 12 show how varying the concentrations of CO_2, N_2O and CH_4 affect the filtered spectral fluxes at the mesopause altitude, $z_{mp} = 86$ km. Expanded views of the differences between the flux for standard and doubled concentrations of greenhouse gases are shown in Fig. 13, where we display

$$\langle \Delta \tilde{F}^{\{i\}}(z_{mp}, 2)\rangle = \langle \tilde{Z}^{\{i\}}(\nu, z_{mp}, 1)\rangle - \langle \tilde{Z}^{\{i\}}(\nu, z_{mp}, 2)\rangle \qquad (83)$$

The frequency-integrated differences

$$\Delta F^{\{i\}}(z_{mp}, 2) = \int_0^\infty d\nu \langle \Delta \tilde{F}^{\{i\}}(z_{mp}, 2)\rangle, \qquad (84)$$

are discussed in more detail in connection with (106).

3.4 Altitude dependence of Z and R

Integrating spectral fluxes, $\tilde{Z}$, like those of Fig. 9, over all frequencies in accordance with (48) gives Z, the frequency-integrated flux shown in the middle panel of Fig. 14. The
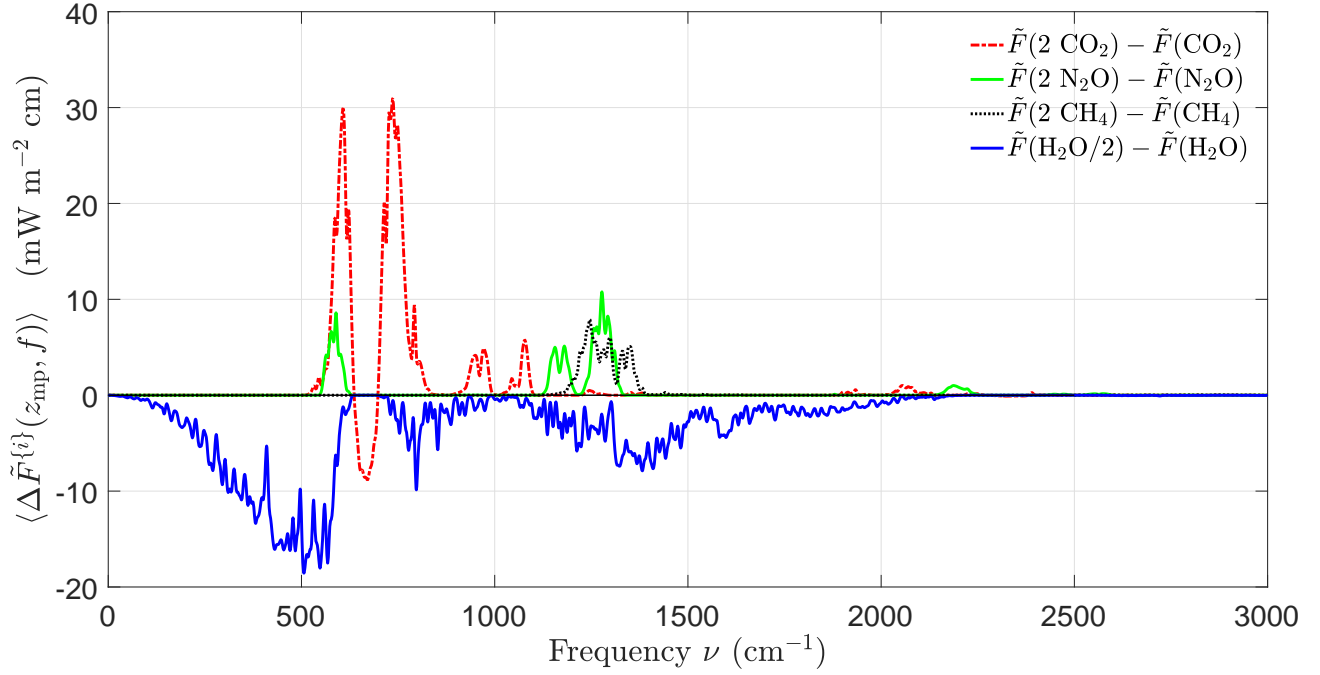
Figure 13: Spectral forcing increments (83) for doubled concentrations of greenhouse gases. These are the magnified differences between the black and red curves of Figs. 10–12. The frequency integrals (84) are tabulated in Table 2. For most frequencies $\langle \Delta \tilde{F}^{\{i\}}(z_{\mathrm{mp}}, 2) \rangle$ is positive. This is because doubling the concentrations of greenhouse gases shifts the emission heights z_e of (76) to higher, colder altitudes in the troposphere. An exception is the band of frequencies near the center of the exceptionally strong bending-mode band of CO_2 at 667 cm^{-1}. Here the emission heights move to higher, warmer altitudes of the stratosphere, where molecules can more efficiently radiate heat to space.

calculations used the temperature profile of Fig. 2, which is shown in the left panel of Fig. 14. The heating rate, $R = -dZ/dz$, shown in the right panel, is negative from the surface to the lower stratosphere, above which the rate is nearly zero. Radiation normally cools the atmosphere, especially the troposphere. An exception is the narrow spike of heating near the tropopause, caused by the convergence of upwelling flux from the troposphere and downwelling flux from the stratosphere at the unrealistically sharp break in the temperature lapse rate.

In steady state, upward transport of sensible and latent heat from the solar-heated surface by atmospheric motions is the main mechanism for replenishing heat radiated to space by greenhouse molecules in the troposphere. Absorption of sunlight, for example, by H_2O, CH_4 and O_3 molecules, and by particulates also contribute to heating. Radiative cooling of tropospheric air parcels allows them to contract and become heavy enough to sink back to the surface, where they pick up enough surface heat to become buoyant, float upward, and continue the convection cycle. Without radiative cooling, convection would cease. And convection would also cease without surface heating by solar radiation. The "heat engine" of the atmosphere absorbs heat from the Sun and, with the aid of greenhouse gases, rejects
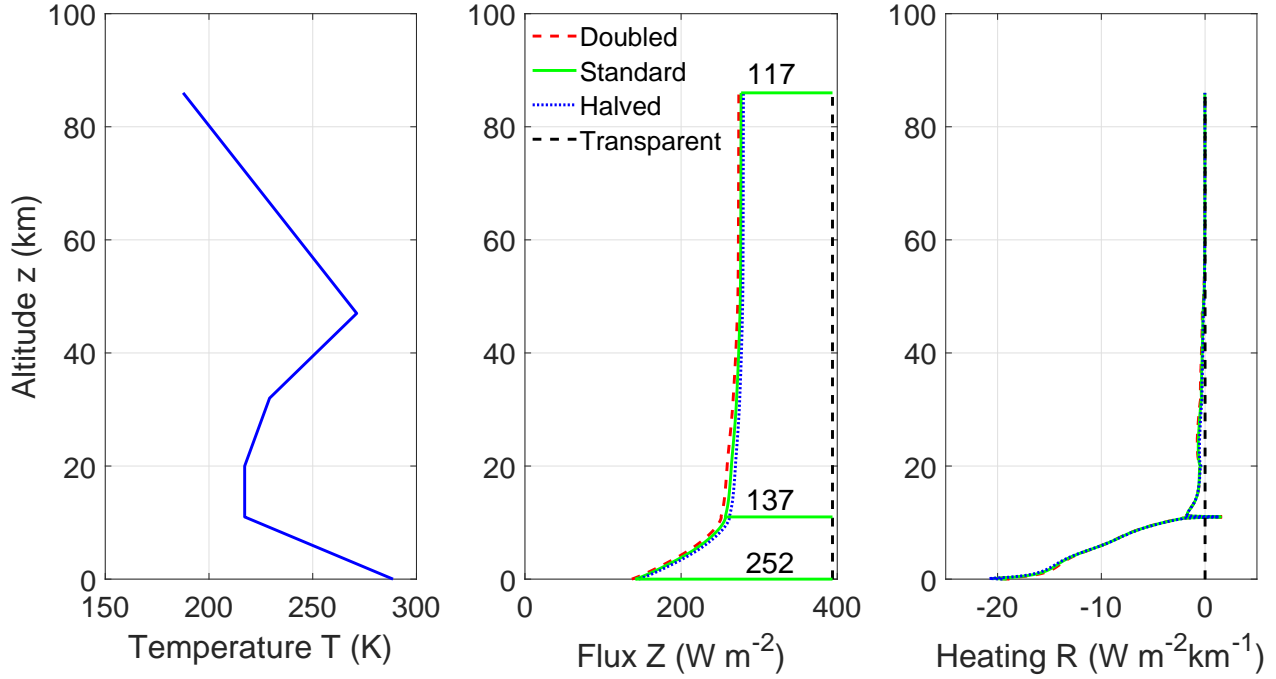
Figure 14: **Left.** Midlatitude standard temperature profile. **Middle.** Altitude dependence of frequency-integrated flux Z of (48). The flux for three concentrations of CO_2 are shown, the standard concentration, $C_{sd}^{\{i\}} = 400$ ppm of Fig. 2, twice and half that value. The other greenhouse gases have the standard concentrations of Fig. 2. The vertical dashed line is the flux $\sigma_{SB}T_0^4 = 394$ W m^{-2} for a transparent atmosphere with a surface temperature $T_0 = 288.7$ K. The forcings F_s that follow from (49) at 0 km, 11 km and 86 km are also indicated (in W m^{-2}) as 252, 137 and 117. The calculated mesopause flux, 277 W m^{-2} is comparable to the observed annual averages of Fig. 1. **Right.** Altitude dependence of the heating rate R of (50). Doubling or halving the standard concentrations of CO_2 makes almost no difference.

most of this heat as radiation to cold space. Some of the difference between the absorbed solar heat and the heat radiated to space is converted, through buoyant forces, into the work that drives the general circulation of the atmosphere[42].

3.5 Latitude dependence of Z and R

Thermal radiative fluxes depend on latitude. They are larger near the equator where the surface is relatively warm than near the poles, where the surface is colder and where wintertime temperature inversions often form in the lower troposphere. For example, Fig. 15 is the analog of Fig. 14 but for Antarctica.

For Fig. 15 we used a five-segment temperature profile with altitude breakpoints at $z = [0, 2.5, 8, 25, 47, 86]$. The low tropopause at 8 km is characteristic of the nighttime poles, as is the strong, wintertime temperature inversion, peaking at 2.5 km. The lapse rates between the break points were $-dT/dz = [-12.5, 2.33, 0, -1.5, 2.145]$ K km^{-1}. The surface
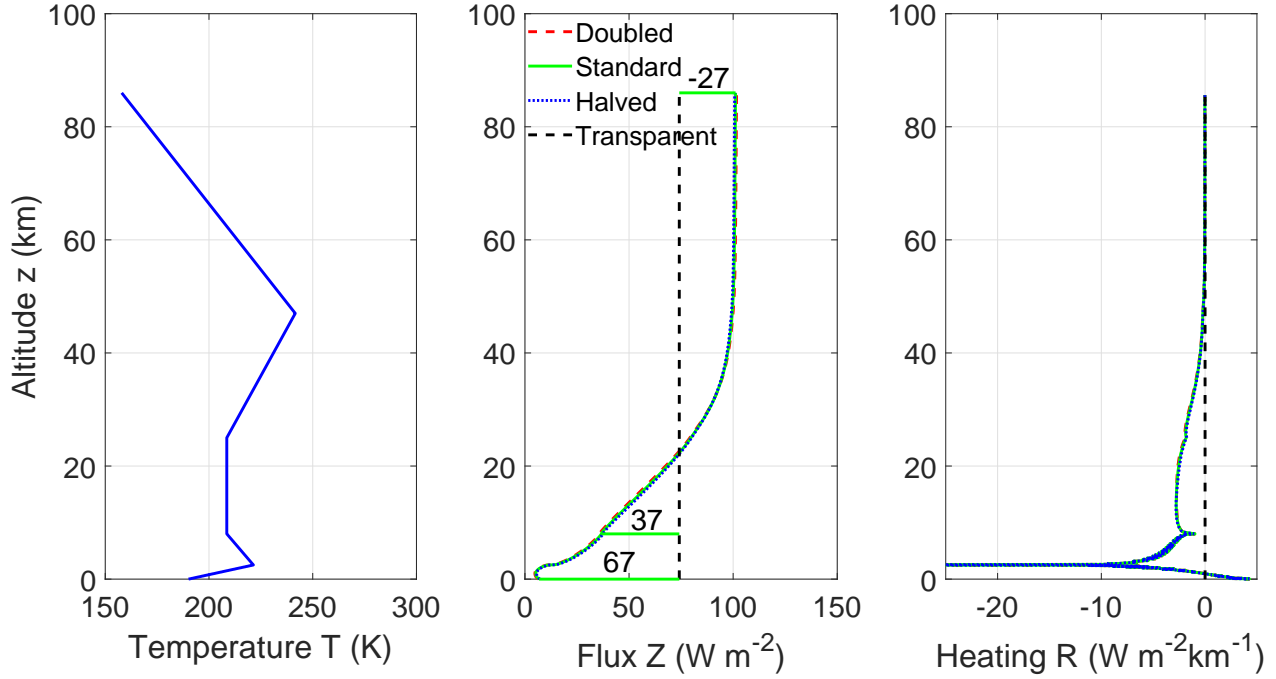
Figure 15: Quantities analogous to those of Fig. 14 at the South Pole. There is a strong temperature inversion at an altitude of 2.5 km above the ice surface. The flux for three concentrations of CO_2 are shown, the standard concentration, $C_{sd}^{\{i\}} = 400$ ppm of Fig. 2, twice and half that value. The other greenhouse gases have the standard concentrations of Fig. 2. The relatively warm greenhouse-gas molecules in the atmosphere enhance the flux to space compared to that which could be produced by a cold surface in a transparent atmosphere[41].

temperature in Antarctica was taken to be $T_0 = 190$ K, and the surface pressure was taken to be only $p_0 = 677$ hPa, because of the high elevation of the ice surface, about 2.7 km above mean sea level.

3.6 Temperature dependence of Z

The temperature dependence and altitude dependence of the frequency-integrated flux Z is shown in Fig. 16. The corresponding fluxes through a transparent atmosphere are shown as the vertical lines on the right of the figure. According to (25), for a transparent atmosphere, where $Z = \sigma_{SB}T_0^4$ the rate of change of flux with temperature is

$$\frac{dZ}{dT_0} = 4\sigma_{SB}T_0^3 = 5.46 \text{ W m}^{-2} \text{ K}^{-1}. \tag{85}$$

The numerical value is for a surface temperature of $T_0 = 288.7$ K. In accordance with (85) the dashed vertical curves of Fig.16 are spaced by approximately 5.5 W m^{-2}.

For an atmosphere with greenhouse gases, the frequency-integrated flux $Z(T_0, z)$ depends on both the surface temperature T_0 and the altitude z, and must be evaluated numerically.

31
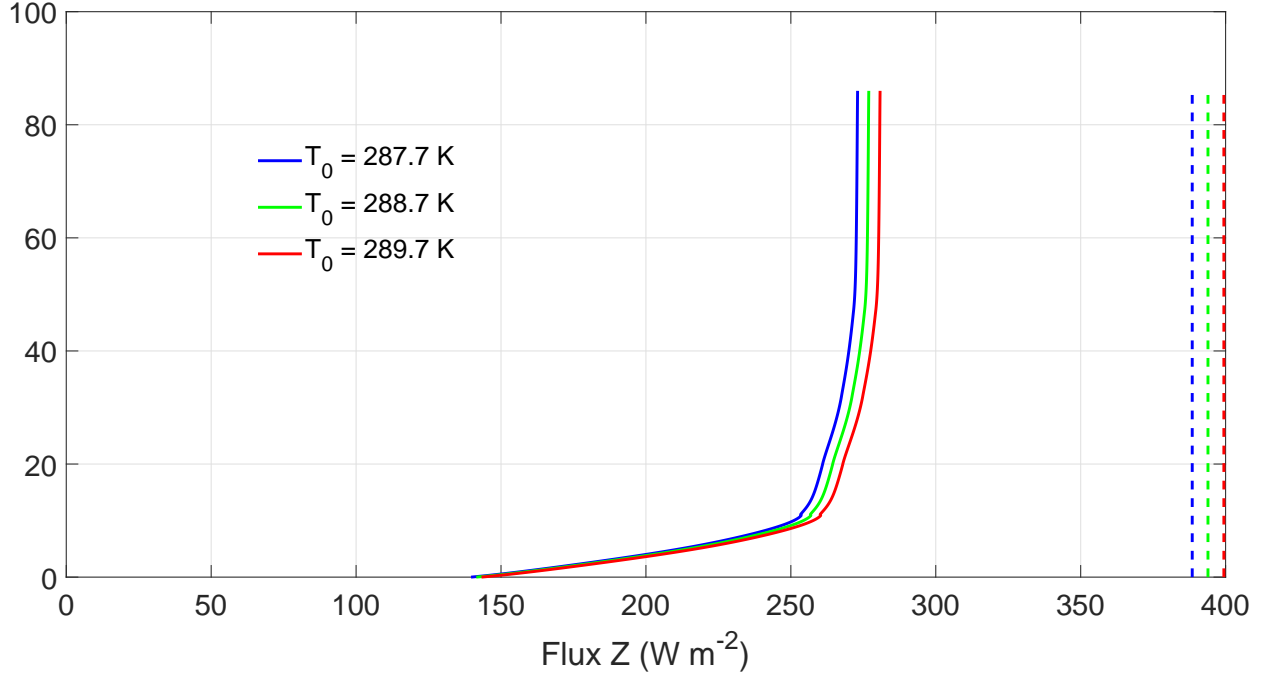
Figure 16: Effect on the upward flux Z of increasing or decreasing the temperature profile of Fig. 2 at all altitudes by an amount $dT = 1$ K. The continuous black curve is the same as the same as the one in the middle panel of Fig. The vertical dashed curves are fluxes, $F = \sigma_{SB}T_0^4$, through a transparent atmosphere.

Numerical calculations, illustrated in Fig. 16, give

$$\frac{\partial Z(T_0, z_{mp})}{\partial T_0} = 3.88 \text{ W m}^{-2} \text{ K}^{-1}. \tag{86}$$

Here the partial derivative with temperature means that the altitude and the concentrations of all greenhouse gases are held constant. No partial derivative is needed for (85) since the upward flux for a transparent atmosphere is determined only by the surface temperature T_0. In accordance with (85) the continuous curves of Fig.16 are spaced by approximately 3.9 W m^{-2} at the mesopause.

According to (85) and (86), to increase the flux to space by the same increment, ΔZ, the required surface temperature increment, ΔT_0, must be a factor of $5.46/3.88 = 1.41$ larger for an atmosphere with greenhouse gases than for a transparent atmosphere. Relatively intense radiation from the warm surface is partially absorbed and replaced by less intense radiation from cooler greenhouse-gas molecules at higher altitudes.

4 Atmospheric Thermodynamics

Radiative energy transfer is closely related to atmospheric thermodynamics and air motions. We briefly discuss some of those connections here.

4.1 Radiative cooling

Consider a small parcel of air of volume ΔV, containing ΔN molecules at a pressure p and temperature T. The heating rate R of (50) will add the heat increment $\delta Q = R \Delta V \delta t$ to the parcel in the time interval δt. According to the first law of thermodynamics, one part of the radiant heat increases the internal energy, ΔU, by an amount $\delta \Delta U = \Delta N c_v k_B \delta T$, where c_v is the specific heat per molecule at constant volume (in units of k_B) and δT is the increase of the parcel temperature. The other part of the radiant heat provides the work, $\delta W = p \, \delta \Delta V$, done on the surrounding air by the expansion, $\delta \Delta V$ of the parcel volume. So the first law of thermodynamics is

$$
\begin{aligned}
R \Delta V \delta t &= \delta U + \delta W \\
&= \Delta N c_v k_B \delta T + p \, \delta \Delta V.
\end{aligned}
\tag{87}
$$

Dividing both sides of (87) by $\Delta V \delta t$ and recalling that the parcel number density is $N = \Delta N / \Delta V$, we find

$$
R = N c_v k_B \frac{\delta T}{\delta t} + p \frac{\delta \ln(\Delta V)}{\delta t}.
\tag{88}
$$

From the ideal gas law, $\Delta V = \Delta N \, k_B T / p$, so

$$
\delta \ln(\Delta V) = \delta \ln(\Delta N \, k_B / p) + \delta \ln T = \delta \ln T.
\tag{89}
$$

Here we noted that under the conditions of near hydrostatic equilibrium that we are considering, $\delta \Delta N = 0$ and $\delta p = 0$ since heating (or cooling) a parcel dry air does not change the number of molecules, ΔN, and does not change the weight of the column of air above, which fixes the pressure p. Combining (88) with (89), and letting $\delta T / \delta t \to \partial T / \partial t$ we find

$$
R = N c_p k_B \frac{\partial T}{\partial t}.
\tag{90}
$$

The specific heat at constant pressure is

$$
c_p = c_v + 1 = \frac{f}{2} + 1 = 3.5,
\tag{91}
$$

where f is the number of degrees of freedom per molecule. In (91) $f = 5$ is the sum of 3 translational and 2 rotational degrees of freedom of the diatomic molecules, N_2 and O_2. There is negligible vibrational excitation. From (90) and the ideal gas law (8), we can write the rate of change of the temperature

$$
\frac{\partial T}{\partial t} = \frac{R}{c_p k_B N} = \frac{RT}{c_p p}.
\tag{92}
$$

The temperature-change rates (92) associated with the radiant heating rates R of Fig. 14 and Fig. 15 are shown in Fig. 17. Since the heating rate R from thermal radiation is negative over most of the atmosphere, so is the temperature-change rate. The rapid increase of these "diabatic" cooling rates with increasing altitude is mainly due to the rapid decrease of the number density N, illustrated in Fig. 3. The local peak at the stratopause is due to a
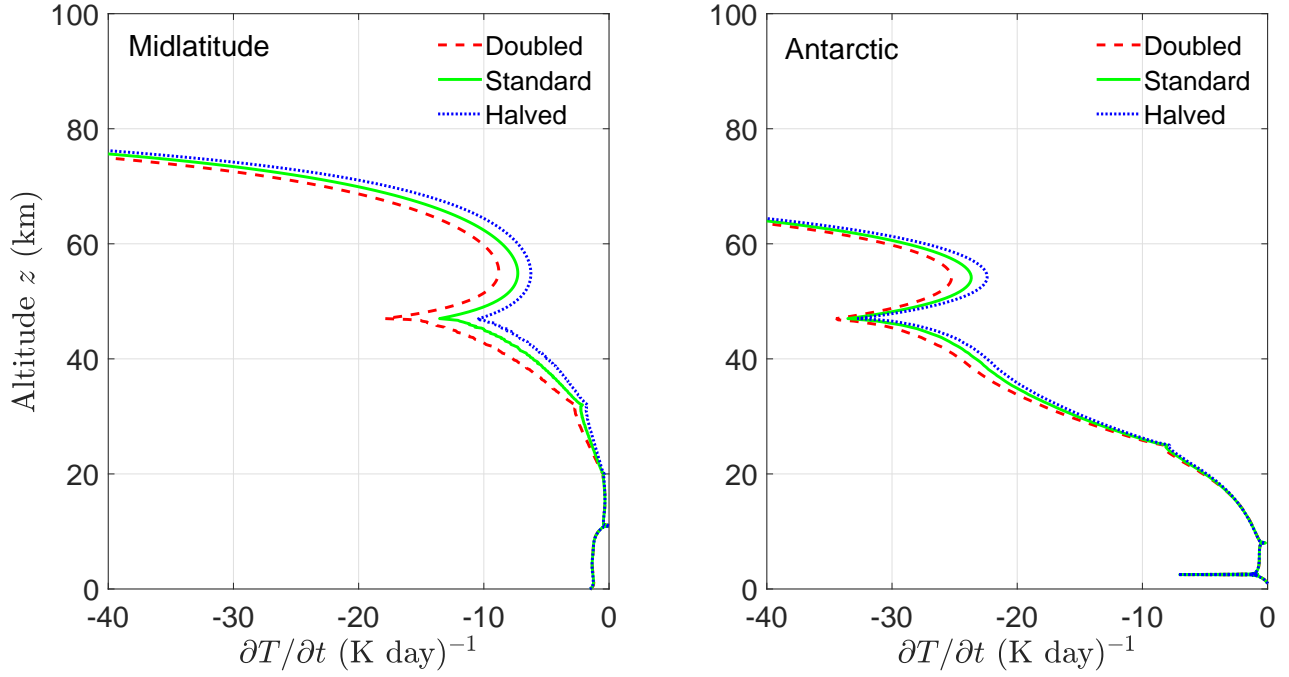
Figure 17: Nighttime radiative cooling rates (92) for the midlatitude temperature and heating-rate profiles of Fig. 14 (left) and the Antarctic profiles of Fig. 15 (right). The cooling rate increases rapidly in the upper stratosphere because of the relatively high temperature near the stratopause, and the decreasing heat capacity of the rarified air. The lower pressure of the stratopause and mesopause over Antractica enhances the radiative cooling there.

peak in R at the local maximum of the temperature, which increases the radiation rate per greenhouse molecule, as discussed in the Appendix. CO_2 and O_3 are responsible for most of thermal radiation absorbed and emitted in the upper atmosphere.

In rocket soundings of the upper stratosphere, Beyers and Miers[43] observed nighttime cooling rates of the order of 10 K day^{-1}, as one would expect from Fig. 17. Fig. 17 also shows that the instantaneous cooling rates, $-\partial T/\partial t$, near the stratopause are noticeably increased by increases in CO_2 concentrations. In contrast, cooling rates in the lower stratosphere and troposphere are slightly decreased by increasing concentrations of CO_2, but the differences are too small to notice in Fig. 17.

4.2 Thermal equilibrium

Averaged over 24 hours, the atmosphere neither heats nor cools very much. So the steady radiative cooling rates shown in in Fig 17 must be nearly balanced, on average, by equal and opposite heating rates from the Sun. Above the tropopause altitude z_{tp}, most of the heat comes from the absorption of solar ultraviolet radiation by ozone, O_3, and oxygen, O_2, molecules. In the troposphere, most of the heat comes from convection of air from the solar-heated surface. Warm air parcels carry heat to higher altitudes, where the $p\,dV$ work

of volume increase dV in the ambient air pressure p adiabatically cools the parcel at the expense of internal energy of the molecules. Thermal radiation removes a relatively small amount of heat and provides diabatic cooling. The relatively large amount of latent heat released when water molecules condense into cloud particulates slows the cooling of rising parcels.

As shown in Fig. 1 there is massive meridional transport of heat from equatorial latitudes, where the yearly-averaged solar heating is maximum, to the the poles, where there is much less solar heating. Mass transport of heat is comparable to radiative transport in Earth's atmosphere. As one can see in Fig.1, near the equator the annual mean absorbed solar power is nearly 320 W m^{-2}, but the thermal radiation to space is only 250 W m^{-2}. So some 70 W m^{-2} of heat must be carried by atmospheric and oceanic circulation toward the both poles. Similarly, near the north pole, the mean solar power is only around 70 W m^{-2}, while the mean thermal radiation to space is around 185 W m^{-2}. Zonal details of heat transport are also important, with radiation dominating in the largely cloud-free Sahara and Arabian deserts, and with substantial reflection of sunlight in marine stratocumulus regions off of Peru and Namibia [2].

4.3   Subsidence

Nighttime radiative cooling will lead to subsidence of the atmosphere, a particularly dramatic phenomenon of polar winters. Using (9) we can write the altitude $z = z(p,t)$ for which the atmosphere has the pressure p, for a given temperature profile $T = T(p,t)$, at time t

$$z = \frac{k_{\mathrm{B}}}{gm} \int_p^{p_0} T' \frac{dp'}{p'}. \tag{93}$$

where $T' = T(p',t)$ and p_0 is the pressure at the surface. We have neglected the slight dependence of the mean molecular mass m on altitude and taken it outside the integral. If the temperature profile is changing with time because of radiative cooling, the altitudes for a given pressure p will also change at the rate

$$\frac{\partial z}{\partial t} = \frac{k_{\mathrm{B}}}{gm} \int_p^{p_0} \frac{\partial T'}{\partial t} \frac{dp'}{p'} = \frac{k_{\mathrm{B}}}{gmc_p} \int_p^{p_0} \frac{R'T'}{(p')^2} dp', \tag{94}$$

where we used (92). To maintain hydrostatic equilibrium, parcels of pressure p will rise or sink with time depending on whether the radiative energy transfer causes expansion or contraction of atmospheric layers at lower altitudes and higher pressures.

4.4   Conservation of energy

Let $\hat{E}$ be the column energy density of the atmospheric molecules. In this section we show that for no horizontal energy exchange, the difference between the infrared flux $Z(0)$ from the surface into the the bottom of the column and the flux, $Z(\infty)$, from the top equals the increase of the internal energy, $\hat{U}$, and gravitational energy, $\hat{G}$, of the molecules.

$$\frac{\partial \hat{E}}{\partial t} = Z(0) - Z(\infty) = \frac{\partial \hat{U}}{\partial t} + \frac{\partial \hat{G}}{\partial t}, \tag{95}$$
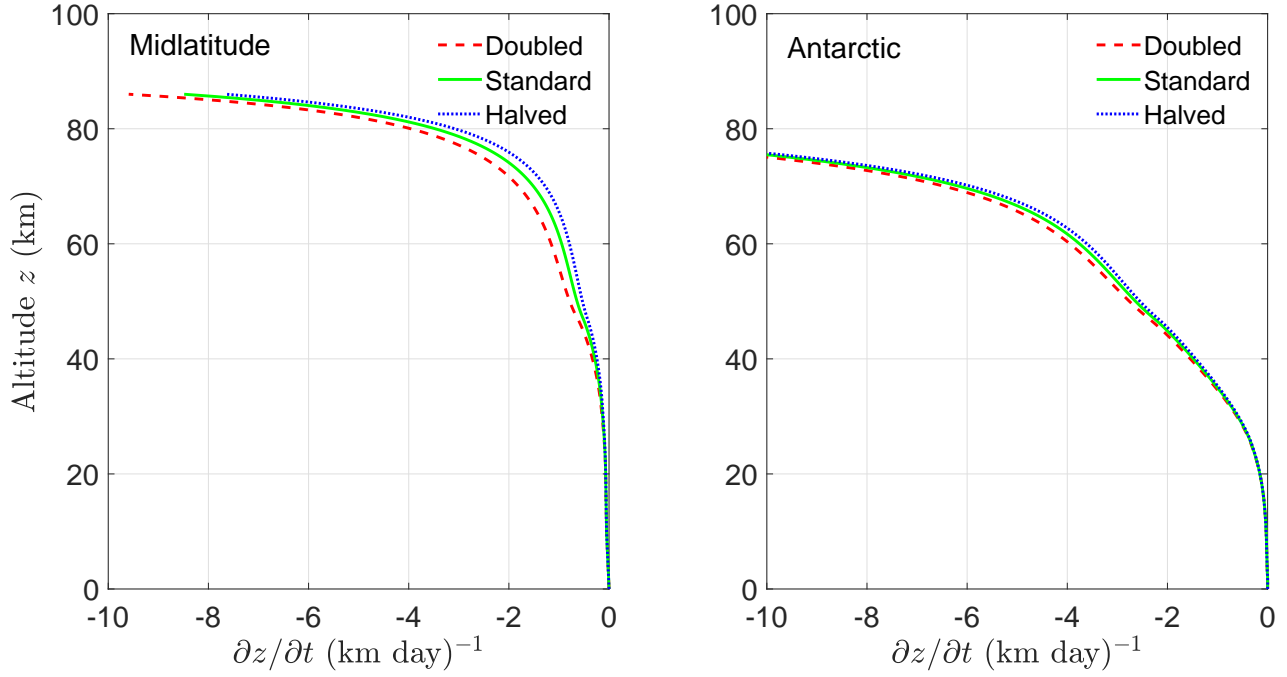
Figure 18: Nighttime subsidence velocities (94) for the midlatitude temperature and heating-rate profiles of Fig. 14 (left) and for the Antarctic profiles of Fig. 15 (right). The subsidence velocities increase with increasing altitude.

From (47) and (90) we find that

$$
\begin{aligned}
Z(0) - Z(\infty) &= -\int_0^\infty \frac{\partial Z}{\partial z} dz = \int_0^\infty R \, dz \\
&= \int_0^\infty c_p k_B N \frac{\partial T}{\partial t} dz = \frac{c_p k_{\mathrm{B}}}{mg} \int_0^{p_0} \frac{\partial T}{\partial t} dp \\
&= \frac{(c_v + 1) k_{\mathrm{B}}}{mg} \int_0^{p_0} \frac{\partial T}{\partial t} dp = \frac{\partial \hat{U}}{\partial t} + \frac{\partial \hat{G}}{\partial t},
\end{aligned}
\tag{96}
$$

In the second line of (96) we used (9) and (8) to transform an integral over altitude increments dz to an integral over pressure increments dp. The temperature $T = T(p,t)$ can be written as a function of pressure p and time t. From (96) we see that the column density of internal energy is

$$
\hat{U} = \frac{c_v k_{\mathrm{B}}}{mg} \int_0^{p_0} T \, dp = \int_0^\infty U \, dz.
\tag{97}
$$

Using (9) with (97) we see that the volume density of internal energy is

$$
U = c_v k_{\mathrm{B}} N T
\tag{98}
$$

In like manner we write column density of gravitational energy as

$$
\hat{G} = \frac{k_{\mathrm{B}}}{mg} \int_0^{p_0} T \, dp = \int_0^\infty G \, dz.
\tag{99}
$$

36

	$F_{\text{sd}}^{\{i\}}(z)$		$\Delta F^{\{i\}}(z,0)$		$\Delta F^{\{i\}}(z,1/2)$		$\Delta F^{\{i\}}(z,2)$	
$i \setminus z$	z_{tp}	z_{mp}	z_{tp}	z_{mp}	z_{tp}	z_{mp}	z_{tp}	z_{mp}
H_2O	81.6	71.6	-72.6	-62.2	-10.4	-7.8	11.2	8.1
CO_2	52.4	38.9	-44.6	-30.2	-5.3	-3.0	5.5	3.0
O_3	6.1	10.5	-4.7	-8.1	-1.8	-2.2	2.5	2.5
N_2O	4.4	4.7	-2.2	-2.2	-0.8	-0.8	1.2	1.1
CH_4	4.2	4.4	-2.1	-2.1	-0.6	-0.6	0.8	0.7
$\sum_i$	148.7	130.1	-126.2	-104.8				
$F_{\text{sd}}(z)$	137	117	137	117				

Table 2: Partial forcings $F_{\text{sd}}^{\{i\}}(z)$ of (104) and partial forcing increments $\Delta F^{\{i\}}(z, f)$ of (106), all in units of W m^{-2}, at the altitudes $z_{\text{tp}} = 11$ km of the tropopause and $z_{\text{mp}} = 86$ km of the mesopause. The last row contains the forcings $F_{\text{sd}}(z)$ of (103), shown in Fig. 14, when all greenhouse molecules are present simultaneously at their standard column densities $\hat{N}_{\text{sd}}^{\{i\}}$. Because of the overlapping absorption bands, $\sum_i F_{\text{sd}}^{\{i\}}(z) > F_{\text{sd}}(z)$, and $-\sum_i \Delta F^{\{i\}}(z, 0) < F_{\text{sd}}(z)$.

The volume density of gravitational energy is

$$G = mgzN. \tag{100}$$

To prove (100) we note that

$$\frac{k_{\text{B}}}{mg} \int_0^{p_0} T \, dp = k_{\text{B}} \int_0^{\infty} TN \, dz = \int_0^{\infty} p \, dz$$
$$= \int_0^{p_0} z \, dp = \int_0^{\infty} mgzN \, dz. \tag{101}$$

Integration by parts leads from the first line of (101) to the second.

For the hypothetical, one-dimensional model of this section, the nighttime cooling and subsidence of the atmosphere, shown by Fig. 17 and Fig. 18, diminish the internal and gravitational energy of a column of air by just enough to supply the net thermal energy radiated away. For the real atmosphere, horizontal pressure gradients generated by the solar heating and radiative cooling discussed here, together with the rotation of the Earth, lead to meridional (north-south) and zonal (east-west) motions. These are the main drivers of atmospheric tides, which have been discussed by Chapman and Lindzen [44] and of global circulation of the atmosphere and oceans.

5 Concentration Dependence of Forcing

The frequency-integrated forcing, F, of (49) depends on the altitude z and on the column densities $\hat{N}^{\{i\}}$ of (11).

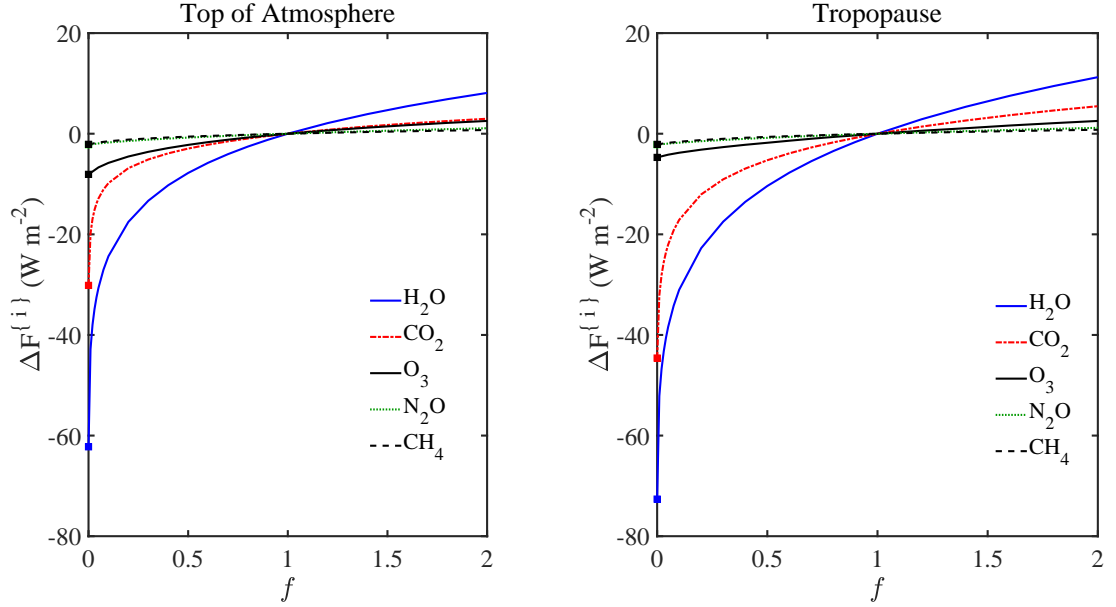$$F = F(z, \hat{N}^{\{1\}}, \ldots, \hat{N}^{\{n\}}). \tag{102}$$

Figure 19: Partial forcing increments $\Delta F^{\{i\}}$ of (106) for the most important greenhouse gases versus the multiplicative factor, $f = N^{\{i\}}/N_{sd}^{\{i\}}$. At the standard column densities, with $f = 1$, the incremental forcings are well into the saturation regime, with $d\Delta F^{\{i\}}(1)/df < d\Delta F^{\{i\}}(0)/df$ for all greenhouse gases. For the most abundant greenhouse gases, $i = H_2O$ and $i = CO_2$, the saturation effects are extreme, with per-molecule forcing powers suppressed by four orders of magnitude at standard concentrations ($f = 1$) with respect to the low-concentration, optically-thin limit ($f = 0$). For CO_2, N_2O, and CH_4, the areas bounded by the green and black curves of Figs. 10 – 12 give the values, $-\Delta F^{\{i\}}$ for $f = 0$, and the areas bounded by the black and red curves give $\Delta F^{\{i\}}$ for $f = 2$, as discussed for Fig. 13. See the text and Table 2 for more details.

Here n is the number of greenhouse gases ($n = 5$ in this paper). We assume that the temperature T and volume densities $N^{\{i\}}$ have the same altitude profiles as in the midlatitude example of Fig. 2. An important special case of (102) is the forcing, F_{sd}, when each greenhouse gas i is present at its standard column density $\hat{N}_{sd}^{\{i\}}$ of Table 1,

$$F_{sd}(z) = F(z, \hat{N}_{sd}^{\{1\}}, \ldots, \hat{N}_{sd}^{\{n\}}). \tag{103}$$

A second special case of (102) is the hypothetical, per-molecule standard forcing, $F_{sd}^{\{i\}}$, when the atmosphere contains only molecules of type i at their standard column density, $\hat{N}^{\{i\}} = \hat{N}_{sd}^{\{i\}}$, and the concentrations of the other greenhouse vanish, $\hat{N}^{\{j\}} = 0$ if $j \neq i$.

$$F_{sd}^{\{i\}}(z) = F(z, 0, \ldots, 0, \hat{N}_{sd}^{\{i\}}, 0, \ldots, 0). \tag{104}$$

We define the forcing power per added molecule as

$$P^{\{i\}}(z, \hat{N}^{\{1\}}, \ldots, \hat{N}^{\{n\}}) = \frac{\partial F}{\partial \hat{N}^{\{i\}}}. \tag{105}$$

The densities of greenhouse gases j with $j \neq i$ are held constant in the partial derivative of (105). If the units of F are taken to be W m^{-2} and the units of $\hat{N}^{\{i\}}$ are taken to be molecules m^{-2}, then the units of $P^{\{i\}}$ will be W molecule^{-1}.

We define a finite forcing increment for the ith type of greenhouse molecule as

$$\Delta F^{\{i\}}(z, f) = F(z, \hat{N}_{\text{sd}}^{\{1\}}, \ldots, \hat{N}_{\text{sd}}^{\{i-1\}}, f\hat{N}_{\text{sd}}^{\{i\}}, \hat{N}_{\text{sd}}^{\{i+1\}}, \ldots, \hat{N}_{\text{sd}}^{\{n\}}) - F_{\text{sd}}. \tag{106}$$

Differentiating (106) with respect to f we find

$$\frac{\partial \Delta F^{\{i\}}}{\partial f}(z, f) = \hat{N}_{\text{sd}}^{\{i\}} P_{\text{sd}}^{\{i\}}(z, f), \tag{107}$$

where $P_{\text{sd}}^{\{i\}}(z, f)$ is the forcing power per additional molecule of type i when these molecules have the column density $\hat{N}^{\{i\}} = f\hat{N}_{\text{sd}}^{\{i\}}$ and all other types of greenhouse molecules have their standard column densities.

The forcing increments (106) for the five greenhouse gases considered in this paper are shown as a function of f in Fig. 19. Forcing increments are also tabulated at representative altitudes z and multiplicative factors f in Table 2. At both the top of the atmosphere and at the tropopause, we see that the forcing increment (106) is largest for abundant water molecules, H_2O, and is relatively small for the much more dilute greenhouse gases CH_4 and N_2O. The incremental forcings are all in the saturation regime, with $\partial \Delta F^{\{i\}}/\partial f$ diminishing with increasing f.

Note from Table 2 that doubling or halving the column density of CO_2 changes the forcing F by almost the same amount, either at the tropopause or at the mesopause. This dependence of forcing increments on the logarithm of the column density of CO_2 was first pointed out by Arrhenius[45], who assumed that temperature changes of the atmosphere would be proportional to forcing changes. On page 53 of his popular book, *Worlds in the Making; the Evolution of the Universe* [45], Arrhenius states

> "If the quantity of carbon dioxide in the air should sink to one half its present percentage, the temperature would fall by 4 K; a diminution by one-quarter would reduce the temperature by 8 K. On the other hand any doubling of the percentage of carbon dioxide in the air would raise the temperature of the Earth's surface by 4 K and if the carbon dioxide were increased by four fold, the temperature would rise by 8 K."

Wilson and Gea-Banacloche[46] explain how the approximate dependence of the absorption cross section of CO_2 on frequency ν, $\sigma^{\{i\}} = \sigma_e e^{-\lambda_e|\nu - \nu_e|}$, leads to the logarithmic forcing law articulated by Arrhenius. Here σ_e is the maximum cross section at the center frequency, $\nu_e = 667$ cm^{-1}, of the bending-mode band.

The forcing increments in Table 3 are comparable to those calculated by others. For example, in column 3 we give the increments $\Delta F^{\{i\}}(z, f)$ calculated by Collins et al. [13],

		$\Delta F^{\{i\}}(z,f)$ in W m^{-2}				$\Delta T^{\{i\}}$
		Ref. [13]		This work		in K
i	f	z_{tp}	z_{mp}	z_{tp}	z_{mp}	
H$_2$O	1.06	1.4	1.1	0.9	0.7	0.2
CO$_2$	2	5.5	2.8	5.5	3.0	0.8
N$_2$O	2	1.3	1.2	1.2	1.1	0.3
CH$_4$	2	0.6	0.6	0.8	0.7	0.2

Table 3: Comparison of the forcing increments $\Delta F^{\{i\}}(z,f)$ of Collins it et al.[13] in column 3, and the results of Table 2 and (106) in column 4, at the altitude $z_{\mathrm{tp}} = 11$ km of the tropopause and $z_{\mathrm{mp}} = 86$ km of the mesopause. For H$_2$O, the relative increase, $f = 1.06$, of the column density is approximately that caused by a 1 K increase of the surface temperature.

as estimated from their Table 2 and Table 8. These are the results of averaging 5 separate line-by-line calculations. In addition to line intensities, three of the calculations used a continuum CO$_2$ opacity, and all five used a continuum H$_2$O opacity. The physical origin of these continua is unclear. They are added to make the computer calculations agree better with observations [13, 47]. The forcings calculated in this paper, summarized in column 4, used only lines for the HITRAN data base and no continua. Our values are fairly close to those of Collins et al.[13], with the largest discrepancy for H$_2$O. The mesopause spectral intensities, calculated with only HITRAN lines and with no continuum contributions, are in excellent agreement with satellite measurements over the Sahara Desert, the Mediterranean Sea and Antarctica, as discussed in Section 7.

The three mesopause flux increments $\Delta F^{\{i\}}$ in the fourth column of Table 3 for doubled concentrations of CO$_2$, N$_2$O and CH$_4$ sum to 4.8 W m^{-2}. The calculated flux increment from simultaneously doubling CO$_2$, N$_2$O and CH$_4$ is the slightly smaller value, $\Delta F = 4.7$ W m^{-2}. Similarly, the four mesopause flux increments $\Delta F^{\{i\}}$ in the fourth column of Table 3 for doubled the concentrations of CO$_2$, N$_2$O and CH$_4$ and a factor of $f = 1.06$ increase of H$_2$O concentration sum to 5.5 W m^{-2}. The calculated flux increment from simultaneously doubling CO$_2$, N$_2$O and CH$_4$, and increasing the H$_2$O concentrations by a factor of $f = 1.06$, is the slightly smaller value 5.3 W m^{-2}. The "whole" is less than the sum of the parts, because of the interference of greenhouse gases that absorb the same infrared frequencies.

Table 4 summarizes the forcing powers (105) per additional molecule in units of 10^{-22} W at the tropopause altitude, $z_{\mathrm{tp}} = 11$ km and at the mesopause altitude, $z_{\mathrm{mp}} = 86$ km. The surface temperature was $T_0 = 288.7$ K, and the altitude profiles of temperature and number density were those of Fig. 2. The first column lists the molecules we considered. The numbers in the second column are forcing powers, $P_{\mathrm{ot}}^{\{i\}}(z)$, of (110) in the optically-thin limit. The numbers of the third column are forcing powers $P_{\mathrm{sd}}^{\{i\}}(z,0)$ from (107) for an atmosphere that previously had no molecules of type i (so $\hat{N}^{\{i\}} = 0$) but all other greenhouse molecules had standard concentrations, $\hat{N}^{\{j\}} = \hat{N}_{\mathrm{sd}}^{\{j\}}$ if $j \neq i$. The forcings of the third column are less than those of the second because of interference between absorption by different greenhouse gases. The numbers in the fourth column are the forcing powers $P_{\mathrm{sd}}^{\{i\}}(z,1)$ from (107) when

$i \setminus z$	$P_{\text{ot}}^{\{i\}}(z)$		$P_{\text{sd}}^{\{i\}}(z,0)$		$P_{\text{sd}}^{\{i\}}(z,1)$	
	z_{tp}	z_{mp}	z_{tp}	z_{mp}	z_{tp}	z_{mp}
H_2O	1.49	1.49	1.16	1.19	3.3×10^{-4}	2.5×10^{-4}
CO_2	2.73	3.45	2.24	2.53	9.0×10^{-4}	4.9×10^{-4}
O_3	2.00	5.69	1.68	4.57	3.3×10^{-1}	3.8×10^{-1}
N_2O	1.68	2.24	0.73	0.91	2.1×10^{-1}	2.0×10^{-1}
CH_4	0.51	0.71	0.21	0.27	2.8×10^{-2}	2.6×10^{-2}

Table 4: Forcing powers (105) per additional molecule in units of 10^{-22} W at the altitude $z_{\text{tp}} = 11$ km of the tropopause and $z_{\text{mp}} = 86$ km of the mesopause. The surface temperature was $T_0 = 288.7$ K, and the altitude profiles of temperature and number density were those of Fig. 2. $P_{\text{ot}}^{\{i\}}(z)$ of (110) is for the optically-thin limit. $P_{\text{sd}}^{\{i\}}(z,0)$ from (107) is for an atmosphere that previously had no molecules of type i (so $\hat{N}^{\{i\}} = 0$) but all other greenhouse molecules had standard concentrations. $P_{\text{sd}}^{\{i\}}(z,1)$ from (107) is for a single molecule of type i added to an atmosphere that previously had standard densities for all greenhouse gases.

a single molecule of type i is added to an atmosphere that previously had standard densities for all greenhouse gases, $\hat{N}^{\{j\}} = \hat{N}_{\text{sd}}^{\{j\}}$. Here saturation of the absorption suppresses the per-molecule forcing by about four orders of magnitude for the abundant greenhouse gases H_2O and CO_2. Saturation causes less drastic suppression or per-molecule forcings for the less-abundant O_3, N_2O and CH_4.

5.1 Optically-thin forcing power per molecule

For sufficiently low concentrations of greenhouse gases, the optical depths τ of (21) will be small, $\tau \ll 1$, for all frequencies ν and all altitudes z. Since $E_2(|\tau' - \tau|) \to 1$ for $|\tau' - \tau| \ll 1$, as shown in Fig. 5, for the optically-thin limit we can can write the frequency integral of the spectral forcing (46) at a reference altitude z as

$$
\begin{aligned}
F_{\text{ot}}(z) &= 2\pi \sum_i \int_0^\infty d\nu \left[\int_0^z dz' \, N^{\{i\}'} \sigma^{\{i\}'} [\tilde{B}_0 - \tilde{B}'] + \int_z^\infty dz' \, N^{\{i\}'} \sigma^{\{i\}'} \, \tilde{B}' \right] \\
&= \sum_i \hat{N}^{\{i\}} P_{\text{ot}}^{\{i\}}(z).
\end{aligned}
\tag{108}
$$

Here $N^{\{i\}'} = N^{\{i\}}(z')$, $\sigma^{\{i\}'} = \sigma^{\{i\}}(\nu, z')$, $\tilde{B}_0 = \tilde{B}(\nu, T_0)$, $\tilde{B}' = \tilde{B}(\nu, T')$, $T' = T(z')$ and $T_0 = T(0)$. The forcing power per greenhouse molecule of type i is

$$
P_{\text{ot}}^{\{i\}}(z) = \frac{1}{2} \int_0^z dz' \frac{N^{\{i\}'}}{\hat{N}^{\{i\}}} \left[\Pi^{\{i\}}(T', T_0) - \Pi^{\{i\}}(T', T') \right] + \frac{1}{2} \int_z^\infty dz' \frac{N^{\{i\}'}}{\hat{N}^{\{i\}}} \Pi^{\{i\}}(T', T').
\tag{109}
$$

The mean power absorbed by a greenhouse-gas molecule of temperature T from thermal-equilibrium radiation of temperature T' is

$$
\Pi^{\{i\}}(T, T') = 4\pi \int_0^\infty d\nu \, \sigma(\nu, z) \tilde{B}(\nu, T') = 4\pi \sum_{ul} S_{ul}^{\{i\}} \tilde{B}_{ul}'.
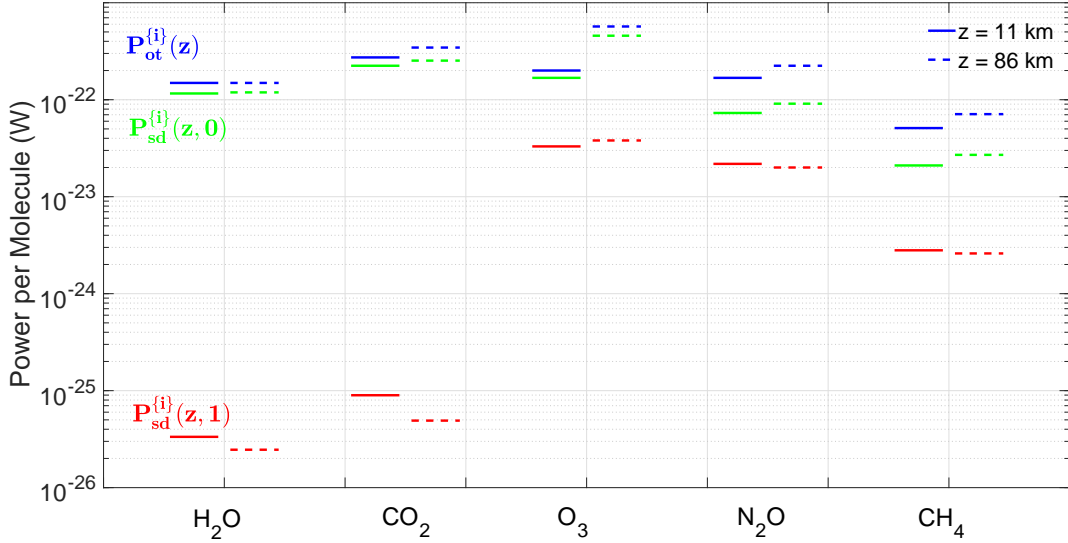\tag{110}
$$

41

Figure 20: A graphical display of the per-molecule forcing powers of Table 4. At standard column densities the (red) powers, $P_{sd}^{\{i\}}(z,1)$, for abundant H_2O and CO_2 are suppressed by four orders of magnitude from their values in the optically thin limit (blue) where the powers are $P_{ot}^{\{i\}}(z)$. This is due to strong saturation of the absorption bands. The effects of saturation (the difference between the blue and red lines) are much less for the minor gases, O_3, N_2O and CH_4. The green lines are the powers per molecule, $P_{sd}^{\{i\}}(z,0)$, of the ith greenhouse gas in its low-concentration limit, but when the forcing power is suppressed by other gases at their standard densities. Interference effects (the difference between the blue and green lines) are more pronounced for the minor greenhouse gases, N_2O and CH_4 than for the major greenhouse gases, H_2O, and CO_2. As one can see from Fig. 6 or Figs. 10 – 12, the strongest bands of O_3 overlap little with those of other greenhouse molecules, which minimizes interference effects.

Here the line intensity of the molecule for the temperature T at altitude z is $S_{ul}^{\{i\}} = S_{ul}^{\{i\}}(T)$, and the Planck spectral radiance of the radiation at temperature T' and frequency ν_{ul} is $\tilde{B}'_{ul} = \tilde{B}(T', \nu_{ul})$. For the special case of $T' = T$ we can substitute (55) into (110) to find

$$\Pi^{\{i\}}(T,T) = \sum_{ul} W_u^{\{i\}} \Gamma_{ul}^{\{i\}} E_{ul}^{\{i\}}. \tag{111}$$

Since we are considering a single isotopologue, we have set $\eta_u = 1$ in (55). The three factors in the summed terms of (111) are: (a) the probability $W_u^{\{i\}} = W_u^{\{i\}}(T)$ of (58) to find the molecule in the upper state u; (b) the radiative decay rate $\Gamma_{ul}^{\{i\}}$ from the upper level u to the lower level l, which can be found from (55); and (c) the mean energy $E_{ul}^{\{i\}}$ of the emitted photon, given by (51). This is obviously the total power radiated by a molecule of temperature T. For a molecule of temperature T in thermal-equilibrium with radiation of the same temperature, the radiative power absorbed by the molecule is equal to the spontaneous radiative power it emits. The forcing powers per molecule discussed above are summarized graphically in Fig. 20.

42

Case	f	θ	δT	$\Delta F_{\mathrm{tp}}^{\{i\}}$	$\Delta F_{\mathrm{mp}}^{\{i\}}$	$\Delta X^{\{i\}}$
(a)	1	0	0	0	0	0
(b)	2	0	0	5.5	3.0	2.5
(c)	2	23.4	0	5.0	5.0	0
(d)	2	23.4	1.3	0	0	0
(e)	2	0	0.8	2.5	0	2.5

Table 5: Numerical details of Fig. 21. The second column has the factor f by which CO_2 concentrations have been multiplied. The third and fourth column list the temperature adjustment parameters, θ and δT of (112), in units of K. In units of W m^{-2}, the numbers of the fifth and sixth columns are the forcing increments, ΔF_{tp} and ΔF_{mp} of (117) and the numbers of the seventh column are the cooling-rate increments $\Delta X^{\{i\}}$ of (116) for the upper atmosphere. In rows (d) and (e), the forcing increments are for a surface with the new temperature $T_0 + \delta T$.

6 Temperature and Forcing

As outlined above, the forcings due to instantaneous changes of greenhouse-gas concentrations can be calculated quite accurately. But the temperature changes induced by the forcings are less clearly defined. This is because various feedbacks come into play to change the temperature profile of the atmosphere. After doubling CO_2 concentrations a new, steady state will eventually be established by these feedback processes. For example, suppose that the new steady state has the same altitude profile for solar heating rates, or for convective heat flow in the horizontal direction, as the initial profile. Then the final flux profile will be the same as the initial flux profile.

Three steps illustrated in Fig. 21 can be used to model how the temperature and flux profiles of the atmosphere return to equilibrium after a change in greenhouse-gas concentrations. Numerical details of Fig. 21 are summarized in Table 5. On the left panel of Fig. 21, the curve labeled (a) is the standard temperature profile of Fig. 2. On the right panel, the curve labeled (a) is an expanded version of the flux, shown in the middle panel of Fig. 14 for the standard concentrations of greenhouse gases, shown on the right panel of Fig. 2. For the curves marked (a), the atmosphere is in thermal equilibrium with solar heating and convective heat transfer balanced by radiative infrared cooling.

Instantaneously doubling the CO_2 concentration from 400 to 800 ppm, with no change in the initial altitude profiles of temperature and other greenhouse-gas concentrations, produces the profiles shown by the lines (b) of Fig. 21. The left panel shows temperature profiles and the right panel shows flux profiles. The new flux profile (b) is not stable for two reasons: (i) the upper atmospheric cooling rate is larger than net heating rate from absorption of ultraviolet sunlight and convection. So the upper atmosphere will start to cool; (ii) the flux to space is less than the total solar flux absorbed, so the atmosphere as a whole will start to heat. Most of the heat capacity is in the troposphere so a very small temperature increase there can more than compensate for large temperature decreases in the upper atmosphere, with its relatively tiny heat capacity.
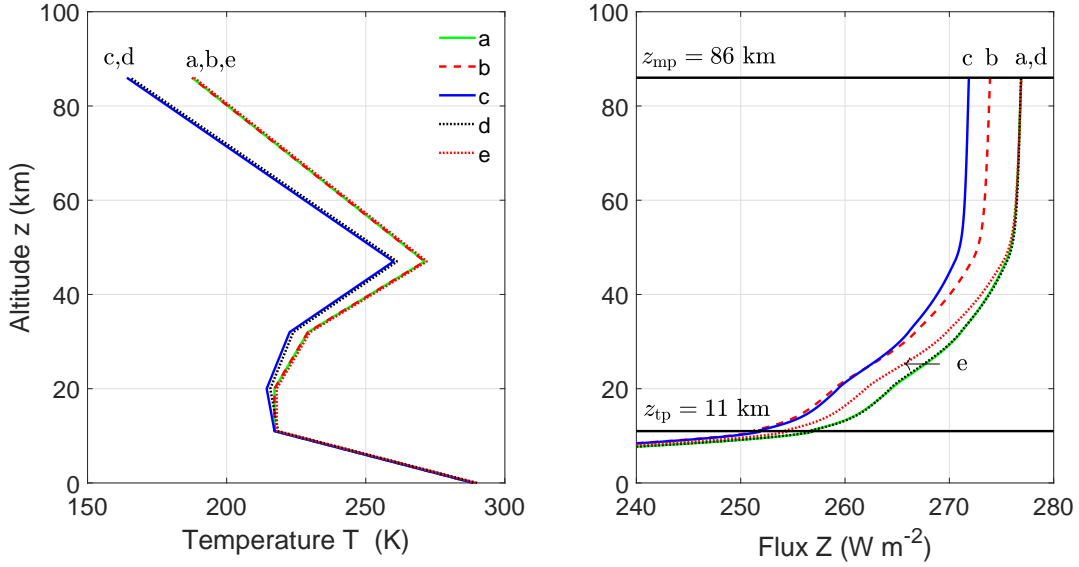
Figure 21: The cases (a), (b), (c), (d) and (e) are summarized in Table 5. (a) The atmosphere is in thermal equilibrium with the initial temperature profile of Fig. 2. Solar and convective heating are balanced by thermal infrared cooling. The CO_2 concentration is $C^{\{i\}} = 400$ ppm; (b) The same temperature profile but with doubled CO_2 concentration, $C^{\{i\}} = 800$ ppm. There is less flux radiated to space and the radiation cooling of the upper atmosphere exceeds the initial value; (c) $C^{\{i\}} = 800$ ppm and with an upper-atmosphere temperature adjustment, (112), parameterized by $\theta = 23.4$ K and $\delta T = 0$ K. This restores the radiative cooling rate to its initial value, but even less flux is radiated to space; (d) $C^{\{i\}} = 800$ ppm and with a temperature adjustment, (112) parameterized by $\theta = 23.4$ K and $\delta T = 1.3$ K. This keeps the cooling in the upper atmosphere equal to its initial value, and it also restores the initial flux to space; (e) $C^{\{i\}} = 800$ ppm and with uniform temperature adjustment, (112), parameterized by $\theta = 0$ K and $\delta T = 0.8$ K to restores the initial flux to space, but leaving excess cooling of the upper atmosphere.

Guided by the cooling rates shown in Fig. 17, we will assume that a few days after a hypothetical instantaneous doubling of CO_2 concentrations, a new, equilibrium temperature profile would be established[5]. We use two temperature-adjustment parameters, θ and δT, both in units of K, to write the new temperature profile as

$$T(z, \theta, \delta T) = T_{\rm sd}(z) - \theta \, \Theta(z) + \delta T. \tag{112}$$

Since the upper atmosphere cools much more rapidly than the lower atmosphere, as shown in Fig. 17, a reasonable approximation for the adjustment profile, $\Theta(z)$, is

$$\Theta(z) = \begin{cases} 0 & \text{for } z < z_{\rm tp} \\ (z - z_{\rm tp})/(z_{\rm mp} - z_{\rm tp}) & \text{for } z \geq z_{\rm tp}. \end{cases} \tag{113}$$

where $z_{\rm mp}$ is the altitude of the mesopause and $z_{\rm tp}$ is the altitude of the tropopause. The last term, δT, of (112) is a uniform temperature increase, δT, at all altitudes, including the surface.

Denote the flux corresponding to the same column densities $\hat{N}^{\{j\}}$ as those of (106), but with the adjusted temperature profile (112) by

$$Z^{\{i\}}(z, f, \theta, \delta T) = Z(z, \hat{N}_{\mathrm{sd}}^{\{1\}}, \ldots, N_{\mathrm{sd}}^{\{i-1\}}, f N_{\mathrm{sd}}^{\{i\}}, N_{\mathrm{sd}}^{\{i+1\}}, \ldots, N_{\mathrm{sd}}^{\{n\}}, \theta, \delta T). \qquad (114)$$

The cooling rate of the upper atmosphere is the difference between the upward flux at the mesopause and the upward flux at the tropopause

$$\begin{aligned} X^{\{i\}}(f, \theta, \delta T) &= Z^{\{i\}}(z_{\mathrm{mp}}, f, \theta, \delta T) - Z^{\{i\}}(z_{\mathrm{tp}}, f, \theta, \delta T) \\ &= \Delta X^{\{i\}}(f, \theta, \delta T) + X^{\{i\}}(1, 0, 0). \end{aligned} \qquad (115)$$

For the midlatitude example of Fig. 14, we see that the standard cooling rate for radiative equilibrium is $X^{\{i\}}(1, 0, 0) = 20$ W m^{-2}. This is equal to the diurnally-averaged ultraviolet heating rate, about 1.4% of the mean solar flux, 1401 W m^{-2}, at Earth's orbit. The incremental cooling rate of the upper atmosphere is

$$\Delta X^{\{i\}}(f, \theta, \delta T) = \Delta F_{\mathrm{tp}}^{\{i\}}(f, \theta, \delta T) - \Delta F_{\mathrm{mp}}^{\{i\}}(f, \theta, \delta T), \qquad (116)$$

where the forcing increments are

$$\begin{aligned} \Delta F_{\mathrm{tp}}^{\{i\}}(f, \theta, \delta T) &= Z^{\{i\}}(z_{\mathrm{tp}}, 1, 0, 0) - Z^{\{i\}}(z_{\mathrm{tp}}, f, \theta, \delta T) \\ \Delta F_{\mathrm{mp}}^{\{i\}}(f, \theta, \delta T) &= Z^{\{i\}}(z_{\mathrm{mp}}, 1, 0, 0) - Z^{\{i\}}(z_{\mathrm{mp}}, f, \theta, \delta T). \end{aligned} \qquad (117)$$

After an instantaneous increase of the concentration of the ith greenhouse gas by a factor f, the temperature adjustment parameter θ that restores radiative equilibrium to the upper atmosphere is the solution of the equation

$$\Delta X^{\{i\}}(f, \theta, 0) = 0. \qquad (118)$$

For the midlatitude example of doubling CO_2 concentrations ($f = 2$), one can solve (118) numerically to find $\theta = 23.4$ K. Using this value of θ we have plotted the temperature profile $T(z, \theta, 0)$ of (112) as curve (c) on the left panel of Fig. 21 and the flux, $Z^{\{i\}}(z, f, \theta, 0)$ of (114) as curve (c) on the right.

As can be seen from Table 5, the temperature and flux profiles, labeled by (c) in Fig. 21, restore radiative equilibrium ($\Delta X^{\{i\}} = 0$) to the upper atmosphere, but they increase the

Latitude	z_{tp}	T_0	θ	δT
Sahara	18	320	25.9	1.7
Midlatitude	11	288.7	23.4	1.3
Antarctica	8	190	6.7	0.3

Table 6: Atmospheric temperature adjustment parameters θ and δT from (112) for the Sahara Desert, Midlatitude and the Antarctic. Also shown are tropospause altitudes z_{tp} and surface temperatures T_0. The tropopause altitudes are given in units of km, and the units of T_0, θ and δT are K. Further details about the altitude profiles of temperature and greenhouse-gas concentrations are contained in Section 7.

forcing at the mesospause from $\Delta F^{\{i\}} = 3$ W m^{-2} to $\Delta F^{\{i\}} = 5$ W m^{-2}, thereby increasing the excess of solar heating over radiative cooling of the atmosphere as a whole. To restore overall thermal equilibrium, we include a uniform temperature shift, given very nearly by

$$\delta T = \Delta F_{\mathrm{mp}}^{\{i\}}(f,\theta,0) \left(\frac{\partial Z}{\partial T_0} \right)^{-1} = 1.3 \text{ K}. \tag{119}$$

where $\partial Z/\partial T_0 = 3.88$ W m^{-2} K^{-1} was given by (86) for midlatitudes, and $\Delta F_{mp}^{\{i\}}(f,\theta,0) = 5$ W m^{-2} is from Table 5. For the temperature adjustment parameters $\theta = 23.4$ K and $\delta T = 1.3$ K, we have plotted the adjusted temperature profile $T(z,\theta,\delta T)$ of (112) as curve (d) on the left panel of Fig. 21 and the flux profile $Z^{\{i\}}(z,f,\theta,\delta T)$ of (114) as curve (d) on the right panel. The flux profile (d) for the fully adjusted atmospheric temperature can hardly be distinguished from the initial flux profile (a).

After doubling the CO_2 concentration, one could restore the flux to space by simply adding a uniform temperature $\delta T = 0.8$ K at each altitude with no upper atmosphere cooling. This is case (e) in Fig. 21 and Table 5. The uniform temperature adjustment is so small that it can hardly be recognized on the left panel of Fig. 21, although the corresponding flux change can be seen clearly on the right panel. The profile (e) has excess cooling of the upper atmosphere, which would cause the temperature to decrease toward the profile of (d).

In summary, for the clear-sky, midlatitude example discussed in this section, doubling CO_2 concentrations, from 400 ppm to 800 ppm, causes substantial cooling of the upper atmosphere, a temperature drop of 23.4 K, at the mesopause. It also causes a modest warming, 1.3 K, of the troposphere. We have done similar calculations for temperature profiles over the Sahara and the winter Antarctic, discussed in connection with Fig. 22 and the results are summarized in Table 6.

7 Comparison of Model Intensities to Satellite Observations

An important issue is the validity of a model. The gold standard is how well model results agree with observations or with experiment. The most important quantity for heat transfer is the spectral flux $\tilde{Z}$. But $\tilde{Z}$ cannot be measured in any straightforward way. High-resolution spectrometers measure the spectral intensity, $\tilde{I}$, propagating into a small element of solid angle, $d\Omega$. In principle, one could select solid angle increments, $\delta\Omega_i$ centered on colatitude angles θ_i and azimuthal angles ϕ_i, such that $\sum_i \delta\Omega_i = 4\pi$. One could then use a high-resolution spectrometer to measure the spectral intensities $\tilde{I}_i$ along each sample direction and numerically estimate the spectral flux as $\tilde{F} = \sum_i \tilde{I}_i \cos\theta_i \delta\Omega_i$ of (16). But this "Gedankenexperiment" is not practical. Precise measurements of frequency-integrated forcings F or heating rates, $R = -\partial Z/\partial z$ are also impractical. Comparisons of spectral fluxes $\tilde{Z}$ calculated by different modeling groups, like those of Table 3, are sometimes used as a gauge of validity. But this is not the same as a comparison with observational or experimental data.

Unlike spectral fluxes, $\tilde{Z}$, spectral intensities, $\tilde{I}$, can be measured very precisely. The modeling of $\tilde{Z}$ and $\tilde{I}$ is done in very similar ways. The exponential integral, $2E_3(\tau)$, of (44)
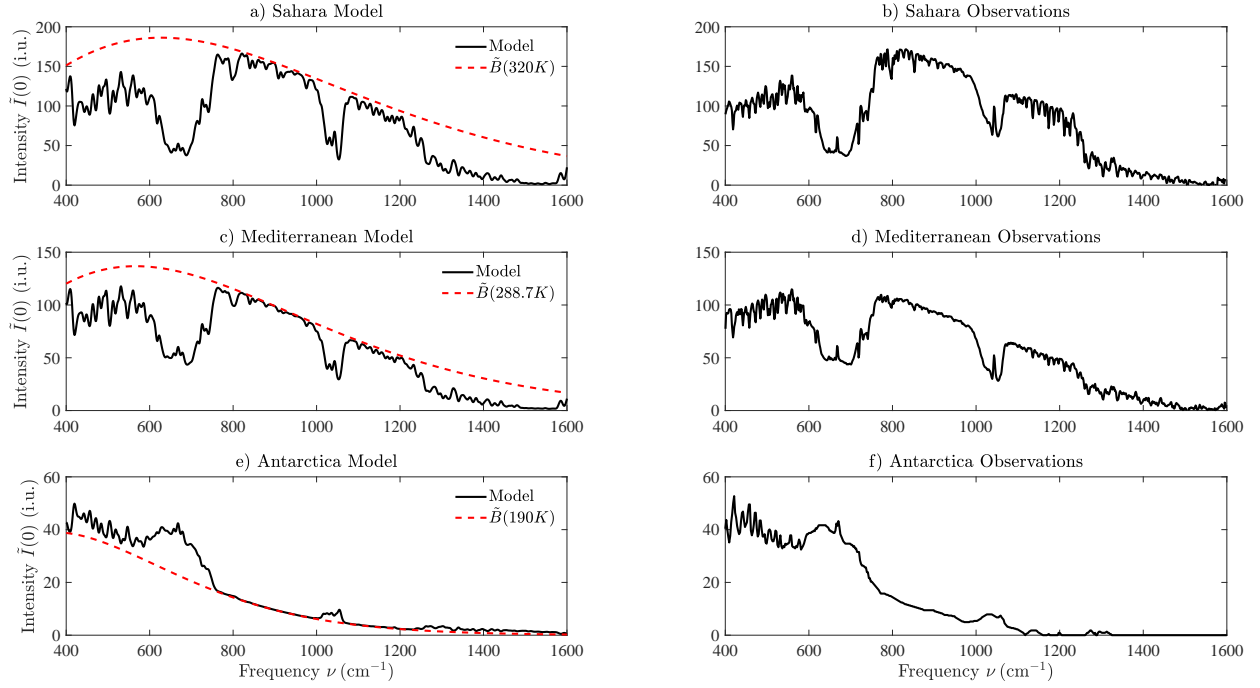
Figure 22: Vertical intensities $\tilde{I}(0)$ at the top of the atmosphere observed with a Michaelson interferometer in a satellite[40], and modeled with (34): over the Sahara desert, the Mediterranean and Antarctica. The intensity unit is 1 i.u. = 1 mW m^{-2} cm sr^{-1}. Radiative forcing is negative over wintertime Antarctica since the relatively warm greenhouse gases in the troposphere, mostly CO_2, O_3 and H_2O, radiate more to space than the cold ice surface, at a temperature of $T = 190$ K, could radiate through a transparent atmosphere.

that describes the attenuation, at the optical depth τ, of the spectral flux, $\tilde{U}_0 = \pi\tilde{B}_0$, from the surface, is closely analogous to the exponential $e^{-\tau}$ of (32), that describes the attenuation of the surface spectral intensity $\tilde{I}_0 = \tilde{B}_0$, propagating vertically with $\varsigma = 1$. The function $2E_2(\tau - \tau')$ of (44), that describes the attenuation of the spectral flux, $\tilde{Z}$, generated by greenhouse gases at the optical depth $\tau' < \tau$ is analogous to the factor $e^{-(\tau-\tau')}$ of (33) for the corresponding contributions to $\tilde{I}$.

Fig 22 shows vertical spectral intensities, $\tilde{I}(0)$, measured with a Michaelson interferometer from a satellite over the Sahara Desert, the Mediterranean Sea and Antarctica. The figure also shows values of the vertical intensity, $\tilde{I}$, calculated with (34). For the Mediterranean, we used the five-segment temperature profile of Fig. 2. For the Sahara and Antarctica we used analogous profiles with different parameters. The altitude breakpoints for the Sahara were at $z = [0, 18, 20, 32, 47, 86]$ km. The high tropopause at 18 km is characteristic of near-equatorial latitudes. For Antarctica the altitude breakpoints were $z = [0, 2.5, 8, 25, 47, 86]$. The low tropopause at 8 km is characteristic of the nighttime poles, as is the strong, wintertime temperature inversion, peaking at 2.5 km. The lapse rates between the break points were $-dT/dz = [6.5, 0, -1, -3.8, 2.145]$ K km^{-1} for the Sahara and $-dT/dz = [-12.5, 2.33, 0, -1.5, 2.145]$ K km^{-1} for Antarctica. The surface temperature in

47

the Sahara was taken to be $T_0 = 320$ K (very hot) and the surface temperature in Antarctica was taken to be $T_0 = 190$ K (very cold). The surface pressure in the Sahara and the Mediterranean was taken to be $p_0 = 1013$ hPa and the surface pressure in Antarctic was taken to be $p_0 = 677$ hPa, low because of the high elevation of the ice surface, about 2.7 km above mean sea level.

For convenience, we modeled the dependence of the water vapor concentrations $C^{\{i\}}$ on the height z above the surface as

$$C^{\{i\}} = C_0^{\{i\}} e^{-z/z_w}, \tag{120}$$

with a latitude-independent scale height $z_w = 5$ km and with surface concentrations $C_0^{\{i\}} = 31,000$ ppm for the Sahara, $C_0^{\{i\}} = 12,000$ ppm for the Mediterranean, and $C_0^{\{i\}} = 2,000$ ppm Antarctica. For the year 1970 when the satellite measurements were made, we used surface concentrations, in ppm, for CO_2, N_2O and CH_4 of 326, 0.294 and 1.4, with the same relative altitude profile as those in Fig 2. The altitude profile of Fig. 2 for O_3 was used for the Sahara, the Mediterranean and Antarctica.

As can be seen from Fig. 22 the modeled spectral intensities can hardly be distinguished from the observed values. We conclude that our modeled spectral fluxes would also be close to observed fluxes, if a reliable way to measure spectral fluxes were invented.

8 Conclusions

The two goals of this review were: (1) to rigorously review the basic physics of thermal radiation transfer in the cloud-free atmosphere of the Earth; and (2) to present quantitative information about the relative forcing powers of the the naturally-occurring, greenhouse-gas molecules, H_2O, CO_2, O_3, N_2O and CH_4.

Fig. 2 illustrates how the temperature T of the atmosphere and the concentrations $C^{\{i\}}$ of greenhouse gases of type i depend on the altitude z above the Earth's surface. No matter how high the concentration of greenhouse gases, (46) shows that the TOA forcing of an isothermal atmosphere would be zero, since the brightness $\tilde{B}$ at each source altitude z would be equal to the surface brightness $\tilde{B}_0$, and the forcing increment, $d\tilde{F}'$ from molecules in the altitude interval z' to $z' + dz'$ is proportional to $(\tilde{B} - \tilde{B}_0)dz' = 0$. For radiation forcing, the atmospheric temperature profile is as important as greenhouse-gas concentrations.

Modeling calculations were done with the integral forms of the fundamental radiation transfer formulae, (44) for the spectral flux, $\tilde{Z}$, and (34) for the spectral intensity, $\tilde{I}$. We showed that these follow directly from the Schwarzschild equation (27) for an atmosphere with gas molecules in local thermodynamic equilibrium. Greenhouse gas molecules absorb but do not scatter thermal radiation. Vibration-rotation energy imparted to a molecule by an absorbed infrared photon is lost in collisions with other molecules before it can be radiated away.

Radiation transfer calculations are most conveniently done with the vertical optical depth τ of (21) as a measure of altitude z. We showed how the attenuation coefficient $\kappa = \partial\tau/\partial z$ of (20), can be evaluated with the cross sections $\sigma^{\{i\}}$ of (20), expressed with (52) and (53) in terms of the line intensities and other parameters of the HITRAN data base[31]. In our modeling we included over 1/3 million lines from the HITRAN data base for the five most

important greenhouse gases, H_2O, CO_2, O_3, N_2O and CH_4. Efficient algorithms allowed us to carry out the necessary calculation with laptop computers.

Fig. 7 and Fig. 8 show that the spectral flux $\tilde{Z}$ can increase with altitude if the radiation extracts heat from the molecules leading to spectral cooling $\tilde{R} = -\partial\tilde{Z}/\partial z < 0$. In rare cases, the spectral flux $\tilde{Z}$ decreases with altitude, and absorbed radiant energy heats the molecules $\tilde{R} = -\partial\tilde{Z}/\partial z > 0$, as shown in Fig. 8(d) for the lower stratosphere. Here the frequency $\nu = 1016.2$ cm^{-1} is strongly absorbed by ozone, O_3.

Fig. 17 shows that the nighttime temperature drops rapidly from radiation cooling in the upper atmosphere. High altitudes are very sensitive to heating or cooling because of their relatively low density and low specific heat. Fig. 18 shows the nighttime subsidence rates, which also increase with altitude. As shown in Section 4.4, the energy radiated out of the atmosphere at night comes at the expense of internal and gravitational energy of the cooling, subsiding air molecules.

The upward spectral flux, $\tilde{Z}$, "breaks out" at an emission height z_e, given by (76). Emission heights can be near the top of the atmosphere for frequencies in the middle of strong absorption lines. For frequencies with little absorption, the emission heights can be close to, or at the surface. Fig. 9 shows that the spectral flux $\tilde{Z}$ and the spectral intensity $\tilde{I}$ at the top of the atmosphere vary rapidly with radiation frequency ν.

Radiative forcing depends strongly on latitude, as shown in Fig. 14 – 15. Near the wintertime poles, with very little water vapor in the atmosphere, CO_2 dominates the radiative forcing. The radiation to space from H_2O, CO_2 and O_3 in the relatively warm upper atmosphere can exceed the radiation from the cold surface of the ice sheet, and the TOA forcing can be negative.

Fig. 19 with Tables 2 and 4 show that at current concentrations, the forcings from all greenhouse gases are saturated. The saturation of the abundant greenhouse gases H_2O and CO_2 are so extreme that the per molecule forcing is attenuated by four orders of magnitude with respect to the optical thin values. Saturation also suppresses the forcing power per molecule for the less abundant greenhouse gases, O_3, N_2O and CH_4 from their optically-thin values, but far less than for H_2O and CO_2.

Fig. 23 shows that in the optically-thin limit, the magnitude and temperature dependence of the forcing power per molecule and of the power absorbed per molecule from blackbody radiation is described very well by the harmonic oscillator model described in the Appendix. An exception is the asymmetric-top molecule H_2O, the only greenhouse molecule for which pure rotational transitions play a major role in forcing. This is because H_2O has an exceptionally large permanent dipole moment, 1.85 D (1 D = 10^{-18} statC cm). Table 8 shows that for the harmonic oscillator model the vibrational transition moments $M^{\{i\}}$ of all the greenhouse molecules are much smaller, of order of 0.1 D.

Table 2 and Fig. 20 show that the overlap of absorption bands of greenhouse gases causes their forcings to be only roughly additive. One greenhouse gas interferes with, and diminishes, the forcings of all others. But the self-interference of one greenhouse gas with itself, or saturation, is a much larger effect than interference between different gases. Table 4 shows that for optically thin conditions, the forcing power per molecule is about the same for all greenhouse gases, a few times 10^{-22} W per molecule.

Fig. 21 shows that substantial temperature decrease of the upper atmosphere would be needed to restore hypothetical radiative equilibrium there after the instantaneous doubling

of CO_2 concentrations. A much smaller temperature increase of the whole atmosphere is sufficient to bring the heat flux at the mesopause back to its initial value. The forcings associated with these hypothetical temperature adjustments are summarized in Table 5.

Fig. 22 shows that the integral transform (34) used to calculate TOA intensities $\tilde{I}$ with HITRAN line intensities and with no continuum absorption gives results in very close agreement with spectral intensities observed from satellites over climate zones as different as the Sahara Desert, the Mediterranean Sea and Antarctica. One can therefore have confidence in the calculations of spectral fluxes $\tilde{Z}$, which are calculated with the closely analogous integral transform (44).

The most striking fact about radiation transfer in Earth's atmosphere is summarized by Figs. 10–12. Large relative changes of the concentrations of greenhouse gases from current values cause relatively small changes in forcings. Doubling the current concentrations of the greenhouse gases CO_2, N_2O and CH_4 increases the forcings by only a few percent for cloud-free parts of the atmosphere.

A   Appendix: Harmonic Oscillators

To get more insight into the preceding discussions, we can model the absorption and emission of radiation with quantized harmonic oscillators, of degeneracies $d = 1$, $d = 2$ and $d = 3$. The important vibrational modes of H_2O, CO_2, O_3, N_2O and CH_4 are summarized in Table 7. Rotational motion makes little difference to the total power radiated by vibration-rotation transitions, although rotation causes a considerable spread of frequencies, as can be seen in Fig. 6.

The P and R branches of bending-mode bands of the linear molecule CO_2 and of N_2O are rotational Doppler sidebands of the main vibrational frequency. The Q branches have negligible rotational Doppler broadening, since the axis of rotation and axis of vibration are nearly parallel. Rotation of the bent, asymmetric-top molecules, H_2O and O_3 imposes very complicated rotational sidebands onto the vibrational frequencies.

The bent molecules H_2O and O_3 and the linear molecule N_2O have permanent electric dipole moments, and so these molecules have low-frequency, pure rotational bands in addition to the vibrational bands. The pure rotational transitions of O_3 and N_2O contribute negligible amounts to the power radiated per molecules. But for H_2O, most of the power is from the pure-rotation band.

Let the effective mass of the vibrational mode be m, and let the restoring-force constant be k. We can write the Hamiltonian of a non-rotating molecule with a d-fold degenerate vibrational mode as [49]

$$H = \sum_{j=1}^{d} H_j. \tag{121}$$

50

	ν_1	ν_2	ν_3	ν_4
H_2O	3657	1595	3756	
CO_2	**1388**	[667]	2349	
O_3	1103	701	1042	
N_2O	2224	[589]	1285	
CH_4	**2917**	**[1534]**	{3019}	{1306}

Table 7: Vibrational mode frequencies, in cm^{-1}, for the most important greenhouse gases of Earth's atmosphere. Three-fold degenerate modes ($d = 3$) have frequencies in curly brackets $\{\cdots\}$; two-fold degenerate modes ($d = 2$) have frequencies in square brackets $[\cdots]$ and non-degenerate modes ($d = 1$) have frequencies with no brackets. Frequencies of modes for which the transition transition dipole moment M vanishes (for symmetric isotopologues, like $^{16}O\,^{12}C\,^{16}O$ or $^{12}C\,^1H_4$) are written in bold-face.

The Hamiltonian for motion along the jth coordinate axis is

$$
\begin{aligned}
H_j &= -\frac{\hbar^2}{2m}\frac{\partial^2}{\partial x_j^2} + \frac{k}{2}x_j^2 - \frac{\hbar\omega}{2} \\
&= \frac{\hbar\omega}{2}\left(-\frac{\partial^2}{\partial \xi_j^2} + \xi_j^2 - 1\right) \\
&= \frac{\hbar\omega}{2}\left(a_j a_j^\dagger + a_j^\dagger a_j - 1\right) \\
&= \hbar\omega\, a_j^\dagger a_j.
\end{aligned}
\tag{122}
$$

The resonant frequency is

$$
\omega = \sqrt{\frac{k}{m}} = 2\pi c\,\nu.
\tag{123}
$$

The dimensionless displacements are

$$
\xi_j = \frac{x_j}{X},
\tag{124}
$$

where the characteristic length is

$$
X = \left(\frac{\hbar^2}{mk}\right)^{1/4}.
\tag{125}
$$

The annihilation and creation operators for excitations along the jth spatial axis are

$$
a_j = \frac{1}{\sqrt{2}}\left(\xi_j + \frac{\partial}{\partial \xi_j}\right) \quad \text{and} \quad a_j^\dagger = \frac{1}{\sqrt{2}}\left(\xi_j - \frac{\partial}{\partial \xi_j}\right).
\tag{126}
$$

The commutator of the operators (126)

$$
a_j a_j^\dagger - a_j^\dagger a_j = 1,
\tag{127}
$$

51

can be used to derive the last line of (122). The basis states, ϕ_{n,m_n}, of the molecule are the solutions of the eigenvalue equation

$$H\phi_{n,m_n} = E_n\phi_{n,m_n}. \tag{128}$$

Here $n = 0, 1, 2, \ldots$ is the total number of vibrational excitations of the molecule in the level n. The energy of the level is

$$E_n = \hbar\omega n \tag{129}$$

In (122), we have subtracted the zero-point energy, $\hbar\omega/2$ from the Hamiltonians to ensure that $E_0 = 0$.

For $d > 1$ a second quantum number, $m_n = 1, 2, \ldots, g_n$, is needed to denote the independent states with the same energy. Such degenerate states have $n_j = n_j(m_n)$ quanta of excitation along the jth vibrational axis such that

$$n = \sum_{j=1}^{d} n_j. \tag{130}$$

The number of independent, degenerate states for the level n is

$$g_n = \frac{(n + d - 1)!}{n!(d - 1)!}. \tag{131}$$

For example, the bending mode of the CO_2 molecule with a vibrational frequency of $\nu = 667$ cm^{-1} has a degeneracy of $d = 2$, since the molecule can bend in 2 orthogonal directions, labeled by $j = 1$ and $j = 2$. The ground state with $n = 0$ has $[n_1, n_2] = [0, 0]$ and $g_0 = 1$. The first excited state with $n = 1$ has $[n_1, n_2] = [1, 0]$ or $[n_1, n_2] = [0, 1]$ and $g_1 = 2$. The second excited state with $n = 2$ has $[n_1, n_2] = [2, 0]$ or $[n_1, n_2] = [1, 1]$ or $[n_1, n_2] = [0, 2]$ and $g_2 = 3$, *etc.*.

The statistical weight (131) is the coefficient in the power series expansion

$$\frac{1}{(1 - x)^d} = \sum_{n=0}^{\infty} g_n x^n. \tag{132}$$

We can use (129) and (132) to write the partition function (60) as

$$Q = \sum_n g_n e^{-\hbar\omega n/k_B T} = \frac{1}{(1 - e^{-\hbar\omega/k_B T})^d} \tag{133}$$

For future reference, we note that the mean number of excitation quanta can be written as

$$\begin{aligned}
\langle n \rangle &= \frac{1}{Q} \sum_{n=0}^{\infty} n g_n e^{-\hbar\omega n/k_B T} \\
&= \frac{k_B T^2}{\hbar\omega} \frac{\partial}{\partial T} \ln Q \\
&= \frac{d}{e^{\hbar\omega/k_B T} - 1}.
\end{aligned} \tag{134}$$

The basis states of (128) can be written as

$$\phi_{n,m_n} = \frac{(a_1^\dagger)^{n_1}(a_2^\dagger)^{n_2}\cdots(a_d^\dagger)^{n_d}}{\sqrt{n_1!n_2!\cdots n_d!}}\phi_{0,1}. \tag{135}$$

The non-degenerate, ground-state wave function is

$$\phi_{0,1} = \frac{e^{-(\xi_1^2+\xi_2^2+\cdots+\xi_d^2)/2}}{\pi^{d/4}}. \tag{136}$$

For the ground state (136) there is no vibrational excitation along any axis and

$$n_1 = n_2 = \cdots = n_d = 0. \tag{137}$$

We recall that the commutation relation (127) implies that

$$a_j\phi_{n,m_n} = \sqrt{n_j}\,\phi_{n-1,m_{n-1}}, \tag{138}$$

where

$$n_i(m_{n-1}) = n_i(m_n) - \delta_{ij}. \tag{139}$$

Similarly,

$$a_j^\dagger\phi_{n,m_n} = \sqrt{n_j+1}\,\phi_{n+1,m_{n+1}}, \tag{140}$$

where

$$n_i(m_{n+1}) = n_i(m_n) + \delta_{ij} \tag{141}$$

We write the electric-dipole-moment operator of the molecule as

$$\begin{aligned}
\mathbf{M} &= M\sum_{j=1}^{d}\xi_j\mathbf{x}_j \\
&= \frac{M}{\sqrt{2}}\sum_{j=1}^{d}(a_j + a_j^\dagger)\mathbf{x}_j.
\end{aligned} \tag{142}$$

where $\mathbf{x}_j$ is a unit vector along the jth vibrational axis. The magnitude of the moment is the product of the characteristic length of (125) and a charge q,

$$M = qX. \tag{143}$$

For the simplified model of molecules as harmonic oscillators, we see from (129) that natural labels for the energy labels are $u = n = 0, 1, 2, \ldots$, the number of vibrational quanta of the d-dimensional oscillator. For $j > 1$, we will let u_j be the number of quanta of vibrational energy along the jth axis, such that $\sum_j u_j = u$. For $j > 1$ the degeneracy g_n, the number of second quantum numbers m_u, increases with increasing values of n. Eqs. (138) and (140) imply that the matrix elements of the dipole-moment operator (142) differ from zero only if $l = u - 1$. We will use Dirac notation to write the matrix elements as

$$\langle u, m_u|\mathbf{M}|l, m_l\rangle = \int_{-\infty}^{\infty} d\xi_1 \cdots \int_{-\infty}^{\infty} d\xi_d\,\phi_{u,m_u}^*(\xi_1, \ldots, \xi_d)\mathbf{M}\phi_{l,m_l}(\xi_1, \ldots, \xi_d). \tag{144}$$

53

Molecule	ν (cm^{-1})	d	$\langle n \rangle$	Π (p.u.)	$|M|$ (D)	Γ_{ul} (s^{-1})
H$_2$O	1595	1	3.52×10^{-4}	2.45	0.186	21.9
CO$_2$	667	2	7.46×10^{-2}	15.13	0.181	1.53
CO$_2$	2349	1	8.19×10^{-6}	1.63	0.458	425
O$_3$	1103	1	4.17×10^{-3}	14.21	0.273	15.6
O$_3$	701	1	3.13×10^{-2}	1.00	0.065	0.230
N$_2$O	589	2	1.12×10^{-1}	1.99	0.069	0.152
N$_2$O	1285	1	1.65×10^{-3}	5.28	0.194	12.5
N$_2$O	2224	1	1.53×10^{-5}	1.46	0.354	216
CH$_4$	1306	3	4.46×10^{-3}	2.61	0.080	2.25

Table 8: Frequencies ν and degeneracies d from Table 7, excitation quanta $\langle n \rangle$ of (134) and radiated powers $\Pi = \Pi(T, T)$ of (110) with $T' = T$, transition moments $|M|$ from (149), spontaneous decay rates Γ_{ul} of (146) from an excited molecule with one vibrational quantum, $u = 1$, to the ground state with $l = 0$. A temperature of $T = 288.7$ K was assumed for the temperature-dependent quantities, $\langle n \rangle$ and Π. The power unit is 1 p.u. $= 10^{-22}$ W, and the dipole-moment unit is 1 D $= 10^{-18}$ statC cm.

Using (142), and noting that $\nu_{ul} = \nu = \omega/2\pi c$, and $l = u - 1$, we can write the oscillator strength (61) as

$$
\begin{aligned}
f_{ul} &= \frac{4\pi\nu}{3c\,r_e\hbar\,g_l} \sum_{m_u, m_l} \langle u, m_u | \mathbf{M} | l, m_l \rangle \cdot \langle l, m_l | \mathbf{M} | u, m_u \rangle \\
&= \frac{2\pi\nu M^2}{3c\,r_e\hbar g_l} \sum_{m_u} \langle u, m_u | \sum_{j=1}^{d} a_j^\dagger a_j | u, m_u \rangle \\
&= \frac{2\pi\nu M^2}{3c\,r_e\hbar\,g_l} \sum_{m_u} \sum_{j=1}^{d} u_j \\
&= \frac{2\pi\nu M^2 g_u\, u}{3c\,r_e\hbar\,g_l}.
\end{aligned}
\tag{145}
$$

The raising and lowering operators are structured such that $\sum_{m_l} |l, m_l\rangle\langle l, m_l| = 1$ in (145). Substituting (145) into (62) we find the spontaneous decay rate

$$
\Gamma_{ul} = \frac{2\omega^3 M^2 u}{3c^3\hbar}.
\tag{146}
$$

Substituting (145) into (55) and taking $\eta_u = 1$, since we are considering only one species of molecule, we find the line strength

$$
S_{ul} = \frac{8\pi^3 c\nu^4 M^2 W_u\, u}{3\tilde{B}}.
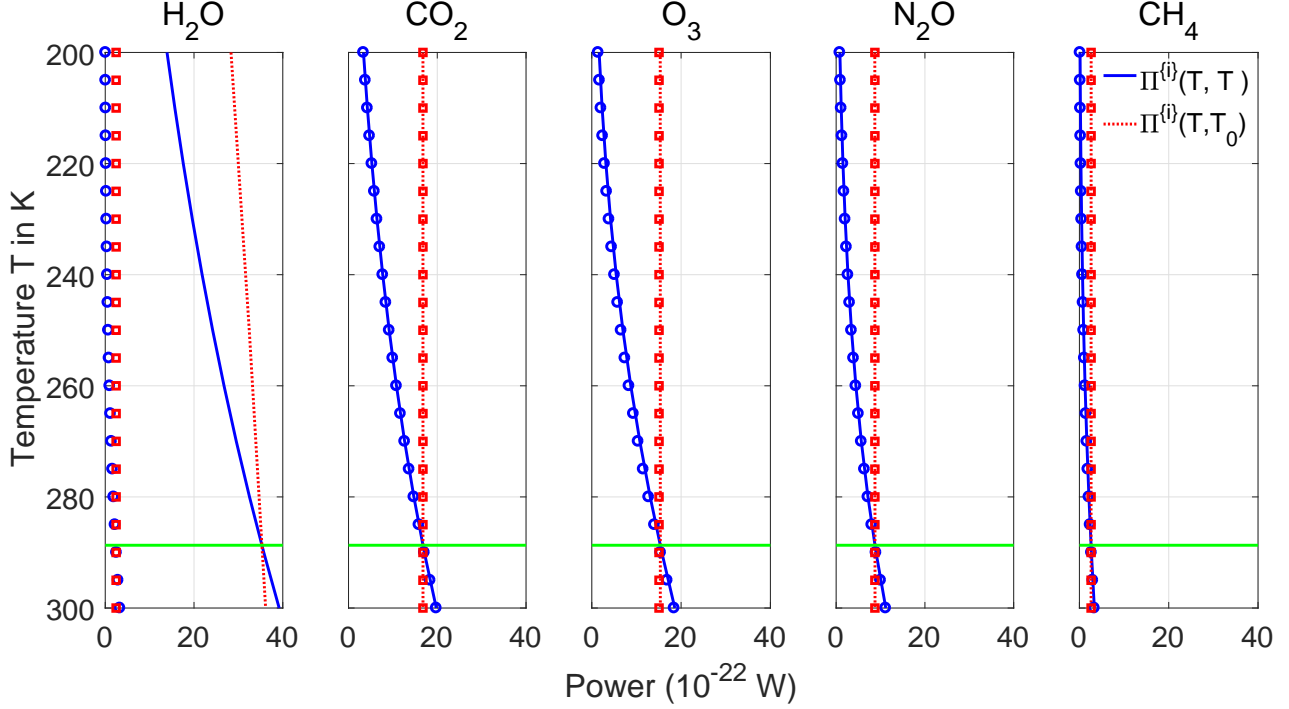\tag{147}
$$

54

Figure 23: The continuous blue lines are the powers $\Pi^{\{i\}}(T, T)$ of (111), emitted by a single greenhouse-gas molecule at the temperature T. The dotted red lines are the powers $\Pi^{\{i\}}(T, T_0)$ of (110) absorbed by a single greenhouse molecule at the temperature T from thermal-equilibrium radiation at the temperature $T_0 = 288.7$ K, shown by the horizontal green line. The blue circles and red squares are the analogous powers from the harmonic oscillator approximation of (148), summed for all vibrational modes of the molecule shown in Table 8 of the Appendix. The emitted and absorbed powers are well modeled with harmonic oscillators for all gases except for the asymmetric-top molecule, H_2O, where most of the power is emitted and absorbed by pure-rotation transitions.

where $\tilde{B} = \tilde{B}(\nu, T)$. The power (110) becomes

$$
\begin{aligned}
\Pi(T, T') &= \frac{\tilde{B}'}{\tilde{B}} \left(\frac{2\omega^4 M^2}{3c^3} \right) \langle n \rangle = \left(\frac{2\omega^4 M^2}{3c^3} \right) \langle n' \rangle \\
&= \left(\frac{2\omega^4 M^2 d}{3c^3} \right) \frac{1}{e^{\hbar\omega/k_B T'} - 1}.
\end{aligned}
\tag{148}
$$

The power (148) absorbed by an ideal, d-dimensional oscillator from thermal radiation at temperature T', is independent of the temperature T of the oscillator.

We can use (148), together with the vibrational quanta per molecule (134) and the power per molecule $\Pi = \Pi(T, T)$ of (110) at the temperature T to find the transition dipole moments in the harmonic oscillator approximation

$$
|M| = \sqrt{\frac{3c^3 \Pi}{2d \langle n \rangle \, \omega^4}}.
\tag{149}
$$

55

Table 8 shows a comparison of the transition dipole moments and other properties for various vibrational modes of the most important greenhouse-gas molecules at a temperature of 288.7 K. The radiation from the modes of O_3 with frequencies $\nu = 1103$ cm^{-1} and $\nu = 1042$ cm^{-1} has been approximated as radiation from a single mode with the frequency, $\nu = 1103$ cm^{-1}, of the stronger band.

The radiated powers Π of (110) at $T = 288.7$ K are all of order 10^{-22} W, and the transition electric dipole moments are all of order one tenth of a Debye unit (1 D $= 10^{-18}$ statC cm). More variable are the mean number of thermally excited vibrational quanta $\langle n \rangle$ of (134), and the spontaneous decay rates Γ_{ul} of (146) for molecules with one quantum of vibrational excitation, $u = 1$.

The total radiated powers per molecule Π, calculated by summing (148) over all molecular modes, are shown as circled points on Fig. 23 for comparison with the value of (110) from summing over tens of thousands of lines. With the exception of H_2O, where the radiated power is dominated by pure rotational transitions, instead of vibration-rotation transitions, the simple, harmonic-oscillator approximation of (148) can hardly be distinguished from the line-by-line value.

Acknowledgements

References

[1] *Radiative Forcing*, IPCC, https://www.ipcc.ch/site/assets/uploads/2018/02/WG1AR5_
Chapter08_FINAL.pdf

[2] S. Dewitte and N.Clerbaux, *Measurement of the Earth Radiation Budget at the Top of the Atmosphere – A Review* Remote Sensing, **9**,1143 (2017).

[3] *Radiation Balance:* PhysicalGeography.net, http://www.physicalgeography.net/fundamentals/chapter

[4] S. Chandrasekhar, *Radiative Transfer*, Dover, New York (1960).

[5] P. M. de F. Forster, R. S. Freckleton and K. P. Shine, *On aspects of the concept of radiative forcing*, Climate Dynamics **13**, 547 (1997).

[6] S. E. Schwartz, *Resource Letter GECC-1: The Greenhouse Effect and Climate Change: Earth's Natural Greenhouse Effect*, Am. J. Phys. **86**, (8), pages 565- 576, August 2018.

[7] S. E. Schwartz, *Resource Letter GECC-2: The Greenhouse Effect and Climate Change: The Intensified Greenhouse Effect*, Am. J. Phys. **86**, (9), pages 645-656, Sept. 2018.

[8] M. Etminan, G. Myhre, E.J. Highwood and K.P. Shine, *Radiative forcing of carbon dioxide, methane and nitrous oxide: A significant revision of the methane radiative forcing*, Geophys. Res. Lett. **43** 12614 (2016); doi: 10.1002/2016GL071930.

[9] K. E. Trenberth and J. T. Fasullo, *Global warming due to increasing absorbed solar radiation*, Geophys. Res. Lett.**36**, L07706 (2009); doi:10.1029/2009GL037527.

[10] R.S. Lindzen, M.-D. Chou, and A. Y. Hou , *Does the Earth have an adaptive infrared iris?*, Bull. Am. Meteorol. Soc. **82**, 417-432 (2001).

[11] G. Myhre and F. Stordal, *Role of spatial and temporal variations in the computation of radiatie forcing and GWP*, J. Geophys. Res. **102**, 11181 (1997).

[12] G. Myhre, E.J. Highwood, K. P. Shine and F. Stordal, *New estimates of radiative forcing due to well-mixed greenhouse gases*, Geophys. Res. Lett. **25**, 2715 (1998).

[13] W.D. Collins *et al. Radiative forcing by well-mixed greenhouse gases: Estimates from climate models in the Intergovernmental Panel on Climate Change (IPCC) Fourth Assessment Report (AR4)*, J. Geophys. Res. **111**, D14317 (2006), doi:10.1029/2005JD006713,

[14] H. Harde, *Radiative and heat transfer in the atmosphere: A comprehensive approach on a molecular basis*, Jour. Atm. Sci. (2013), http://doi.org/10.1155/2013/503727

[15] *The U.S. Standard Atmosphere*, NASA, https://ntrs.nasa.gov/archive/nasa/casi.ntrs.nasa.gov/19770009539.pdf.

[16] R. McClatchey, F. Voltz, R. Fenn, J. Garing and J. Selby, Environ. Res. Paper, AFCRL-782-0497 (1972).

[17] *Radiosondes:* https://www.weather.gov/rah/virtualtourballoon

[18] *Buoyancy:* http://kestrel.nmt.edu/ raymond/classes/ph332/notes/oldstuff/convection/convection.pdf

[19] H. Nebel, P. P. Wintersteiner, R. H. Picard, J. R. Winick, and R. D. Sharma, CO_2 *non-local thermodynamic equilibrium radiative excitation and infrared dayglow at 4.3 µm. Application to Spectral Infrared Rocket Experiment data.* J. Geophys. Res. **99**, 10,409 (1994).

[20] https://www.electronics-notes.com/articles/antennas-propagation/ionospheric/ionospheric-layers-regions-d-e-f1-f2.php

[21] *Stefan-Boltzman constant:* http://scienceworld.wolfram.com/physics/Stefan-BoltzmannLaw.html

[22] J. Lenoble, *Radiative Transfer in Scattering and Absorbing Atmospheres: Standard Computational Procedures*, A. Deepack Publishing (1985).

[23] *Cosmic background radiation:* https://wmap.gsfc.nasa.gov/universe/bb_tests_cmb.html.

[24] *Limb darkening:*, http://astrowww.phys.uvic.ca/∼ tatum/stellatm/atm6.pdf.

[25] *Pyrometers*, https://nvlpubs.nist.gov/nistpubs/Legacy/MONO/nbsmonograph41.pdf.

[26] M. Abramowitz and I. Stegun, *Handbook of Mathematical Functions*, Dover Publications, New York (1965).

[27] K.K. Yoshikawa, *An Iterative Solution of an Integral Equation for Radiative Transfer Using Variational Technique,* https://ntrs.nasa.gov/search.jsp?R=19730020184

[28] J.J. Buglia, *Introduction to the Theory of Atmospheric Radiative Transfer*, https://ntrs.nasa.gov/archive/nasa/casi.ntrs.nasa.gov/19860018367.pdf

[29] A. Einstein, *Zur Quantentheorie der Strahlung*, Physik. Zeitschrift **18**, 121 (1917).

[30] P. A. M. Dirac, *The Principles of Quantum Mechanics*, Oxford University Press, New York (1930).

[31] I. E. Gordon, L. S. Rothman et al., *The HITRAN2016 Molecular Spectroscopic Database*, JQSRT **203**, 3-69 (2017).

[32] W. Voigt, *On the Intensity Distribution Within Lines of a Gaseous Spectrum*, Sitzungsber. Math.-Phys. Kl. Bayer. Akad. Wis. München, p. 603 (1912).

[33] L. S. Rothman, R. L. Hawkins, R. B. Watson and R. R. Gemache, *Energy Levels, Intensities and Linewidths of Atmospheric Carbon Dioxide Bands*, JQSRT, **48**, 537 (1992).

[34] J. A. C. Weideman, *Computation of the complex error function*, SIAM J. Numer. Anal., **31**, 1497 (1994).

[35] M. D. Schwartzkopf and S. B. Fels, *Improvements of the Algorithm for Computing CO_2 Transmissivities and Cooling Rates*, J. Geophys. Res. **90**,10541-10550, (1985).

[36] A. A. Lacis and V. Oinas, *A Description of the Correlated k Distribution Method for Modeling Nongray Gaseous Absorption, Thermal Emission, and Multiple Scattering in Vertically Inhomogeneous Atmospheres*, J. of Geophys. Res., **96**, 9027-9063, (1991).

[37] D. P. Edwards and L. L. Strow, *Spectral line shape considerations for limb temperature sounders*, J. Geophys. Res. **96**, 20859 (1991).

[38] https://www.accessscience.com/content/fraunhofer-lines/757204

[39] *Geostationary Satellite Images*, https://www.ssec.wisc.edu/data/geo-list

[40] R. A Hanel and B. J. Conrath, *Thermal Emission Spectra of the Earth and Atmosphere from the Nimbus 4 Michaelson Interferometer Experiment*, Nature **228**, 143 (1970).

[41] H. Smithüsen, J. Notholt, G. König-Langlo, P. Lemke and T. Jung, *How increasing CO_2 leads to an increased negative greenhouse effect in Antarctica*, Geophys. Res. Lett. **42**, 10422 (2015)

[42] K. A. Emanuel, *The Theory of Hurricanes*, Ann. Rev. Fluid Mech. **23**, 179 (1991).

[43] N. J. Beyers and B. T. Miers, *Diurnal Temperature Change in the Atmosphere between 30 and 60 km Over White Sands Missile Range*, Journal of Atmospheric Sciences, **22**, 262 (1965).

[44] S. Chapman and R. S. Lindzen, *Atmospheric Tides, Thermal and Gravitational*, Springer, 1970

[45] S. Arrhenius, *Worlds in the Making; the Evolution of the Universe*, p. 53, translated by Dr. H. Borns, Harper, New York, London, 1908.

[46] D. J. Wilson and J. Gea-Banacloche, *Simple model to estimate the contribution of atmospheric CO_2 to the Earth's greenhouse effect*, Am. J. Phys. **80** 306 (2012).

[47] D. P. Edwards,*GENL2N A General Line-by-Line Atmospheric Transmittance and Radiance Model*, NCAR Technical Note, NCAR/TN-367+STR (1992).

[48] *Electric Dipole Moments:* https://nvlpubs.nist.gov/nistpubs/Legacy/NSRDS/nbsnsrds10.pdf

[49] A discussion of the algebraic methods used here to analyze harmonic oscillators can be found in many contemporary textbooks, for example, D. J.Griffiths, *Introduction to Quantum Mechanics*, Prentice Hall, Englewood Cliffs, NJ (1995).